Journal of Geophysical Research: Solid Earth

RESEARCH ARTICLE
10.1029/2018JB015490

Lithospheric Structure of Greenland From Ambient Noise and Earthquake Surface Wave Tomography

Maeva Pourpoint[1], **Sridhar Anandakrishnan**[2], **Charles J. Ammon**[2], **and Richard B. Alley**[2]

[1]Department of Earth and Planetary Sciences, Washington University, St Louis, MO, USA, [2]Department of Geosciences, Pennsylvania State University, University Park, PA, USA

Key Points:
- We present a high-resolution shear wave velocity model of Greenland's lithosphere
- Our model provides new constraints on the location of the Iceland plume track beneath Greenland
- We find evidence for a midcrustal low-velocity anomaly beneath the onset of the Northeast Greenland Ice Stream

Correspondence to:
M. Pourpoint,
pourpointmaeva@gmail.com

Citation:
Pourpoint, M., Anandakrishnan, S., Ammon, C. J., & Alley, R. B. (2018). Lithospheric structure of Greenland from ambient noise and earthquake surface wave tomography. *Journal of Geophysical Research: Solid Earth*, *123*, 7850–7876. https://doi.org/10.1029/2018JB015490

Received 14 JAN 2018
Accepted 22 AUG 2018
Accepted article online 29 AUG 2018
Published online 22 SEP 2018

Abstract We present a high-resolution shear wave velocity model of Greenland's lithosphere from regional and teleseismic Rayleigh waves recorded by the Greenland Ice Sheet Monitoring Network supplemented with observations from several temporary seismic deployments. To construct Rayleigh wave group velocity maps, we integrated signals from regional and teleseismic earthquakes with several years of ambient seismic noise and used the dispersion to constrain crustal and upper-mantle seismic shear wave velocity structure. Specifically, we used a Markov Chain Monte Carlo technique to estimate 3-D shear wave velocities beneath Greenland to a depth of 200 km. Our model reveals four prominent anomalies: a deep high-velocity feature extending from southwestern to northwestern Greenland that may be the signature of a thick cratonic keel, a corridor of relatively low upper-mantle velocity across central Greenland that could be associated with lithospheric modification from the passage of the Iceland plume beneath Greenland or interpreted as a tectonic boundary between cratonic blocks, an upper-crustal southwest-northeast trending boundary separating Greenland into two regions of contrasting tectonic and crustal properties, and a midcrustal low-velocity anomaly beneath northeastern Greenland. The nature of this midcrustal anomaly is of particular interest given that it underlies the onset of the Northeast Greenland Ice Stream and raises interesting questions regarding how deeper processes may impact the ice stream dynamics and the evolution of the Greenland Ice Sheet.

1. Introduction

As with most stable continental regions, Greenland has a long and complicated tectonic history. Most of Greenland is dominated by crystalline rocks formed during a succession of orogenic events in the Archean and early Proterozoic and stabilized as part of Laurentia. Subsequent developments, including late Proterozoic to Phanerozoic rifting and basin formation in north-northeast Greenland and Paleozoic orogeny (Ellesmerian fold belt in north Greenland and Caledonian orogenic belt in east Greenland), mostly occurred along the margins of the Greenland shield (Escher & Pulvertaft, 1995; Dawes, 2009; Henriksen et al., 2008, 2009; Roberts & Bally, 2012, Chapters 5 and 11). Late Paleozoic to Mesozoic rift basin formation and sedimentary deposition along the north, east, and west Greenland margins were closely followed by continental breakup and seafloor spreading of the Labrador Sea in the late Cretaceous to early Cenozoic and its abandonment and the opening of the northeast Atlantic during the Paleocene-Eocene transition (Henriksen et al., 2008; Roberts & Bally, 2012; Stemmerik et al., 2013; Surlyk, 1990; Tsikalas et al., 2005). Breakup and seafloor spreading were accompanied by the passage of the Iceland plume beneath Greenland during the late Cretaceous to the late Eocene and an increase in magmatic activity in west and east Greenland and offshore south Greenland, culminating with a voluminous outpouring of basaltic lavas and the formation of the western and eastern Tertiary flood basalt provinces as part of the North Atlantic Igneous Province (Chalmers & Pulvertaft, 2001; Henriksen et al., 2008; Larsen & Saunders, 1998; Larsen et al., 1999; Peace et al., 2017; Roberts & Bally, 2012; Storey et al., 2007; Upton, 1988). The long-term effects of the passage of the Iceland plume beneath Greenland remain debated, and postulated plume tracks vary with plate reconstruction estimates (Doubrovine et al., 2012; Lawver & Müller, 1994; Morgan, 1983; Müller et al., 1993; O'Neill et al., 2005; Steinberger et al., 2004), especially in western Greenland. But it is commonly argued that the high geothermal heat flux (GHF) estimated in central eastern and northeastern Greenland (Buchardt & Dahl-Jensen, 2007; Dahl-Jensen, Gundestrup, et al., 2003; Fahnestock et al., 2001; Greve, 2005; Petrunin et al., 2013; Rezvanbehbahani et al., 2017; Rogozhina et al., 2016; Rysgaard et al., 2018) is the result of long-lived effects of the passage of the Greenland lithosphere over the Iceland mantle plume. Key regions and geologic features are identified in Figure 1.

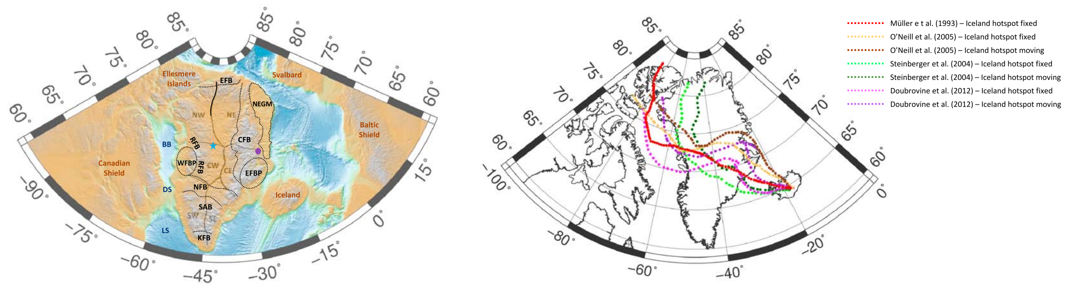

Figure 1. Map of different regions and main geological features referenced in this study (left) and map of proposed Iceland plume tracks relative to Greenland (after Rogozhina et al., 2016). Geological studies by Henriksen et al. (2008, 2009), Dawes (2009) and, Roberts and Bally (2012) were used to delineate the boundaries of main tectonic units. We use the topography of the region (Amante & Eakins, 2009) as our background map. Tectonic provinces: WFBP = Western Tertiary Basalt Province; EFBP = Eastern Tertiary Basalt Province; KFB = Ketilidian Fold Belt; SAB = South Archean Block; NFB = Nagssugtoqidian Fold Belt; RFB = Rinkian Fold Belt; CFB = Caledonian Fold Belt; EFB = Ellesmerian Fold Belt; NEGM = North East Greenland Margin; Major regions: NE = Northeastern Greenland; NW = Northwestern Greenland; CE = Central eastern Greenland; CW = Central western Greenland; SE = Southeastern Greenland; SW = Southwestern Greenland; Seas: BB = Baffin Bay; DS = David Strait; LS = Labrador Sea; GS = Greenland Sea. Other areas of interest: Purple circle—Kong Oscar Fjord. The blue star indicates the location of a cell in central Greenland (74°N and 44.3°W) for which we present detailed results of a 1-D shear wave velocity inversion and MCMC analysis.

Active and passive geophysical experiments have been conducted both offshore and onshore Greenland to better constrain the tectonic framework of its interior. A synthesis of geological (Brooks, 2011; Dawes, 2009; Escher & Pulvertaft, 1995; Hamann et al., 2005; Henriksen et al., 2008, 2009; Koch & Haller, 1971; Larsen et al., 2014; Roberts & Bally, 2012) and geophysical (Funck et al., 2017; Hermann & Jokat, 2016; Schiffer et al., 2015; Schlindwein & Jokat, 1999; Schmirdt-Aursch & Jokat, 2005; Tsikalas et al., 2005; Voss & Jokat, 2007; Voss et al., 2009) studies of the east Greenland margin and shelf identifies pronounced differences in the crustal structure and tectonic evolution north and south of the Kong Oscar Fjord (~73°N, Figure 1), including the presence of magmatic underplating and limited extrusion in the north versus large flood basalt provinces and no underplating in the south. Onshore and offshore active seismic profiles in south Greenland (Alsulami et al., 2015; Chian & Louden, 1992, 1994; Dahl-Jensen et al., 1998; Holbrook et al., 2001; Hopper et al., 2003; Keen et al., 2012; Larsen, 1990; Nielsen et al., 2002) also show contrasting styles of rifted margins from amagmatic to the southwest to volcanic to the southeast.

Information on the crustal structure within the continental margin is available from receiver function and gravity analyses, but the interpretations in some places conflict. *P* and *S* wave receiver function analysis from Kumar et al. (2007) suggests thin crust along the continental margin (30 to 35 km) and fairly homogeneous and thick crust (40 to 45 km) within Greenland’s interior. *P* wave receiver function measurements from Dahl-Jensen, Larsen, et al. (2003) point toward a SW-NE trending boundary separating Greenland into two distinct Proterozoic blocks with crustal thickness estimates ranging from 40–42 km in the north to 45–50 km in the south. Gravity models (Braun et al., 2007; Petrov et al., 2016; Schiffer et al., 2018; Steffen et al., 2017) correlate well with the seismically suggested north-south divide with thicker crust in the southeast and thinner crust in the north. Gravity-derived crustal thickness also tends to be relatively large in central-eastern Greenland.

Previous *P* and *S* wave tomographic studies (Darbyshire et al., 2004; Jakovlev et al., 2012; Lebedev et al., 2017; Pilidou et al., 2004; Rickers et al., 2013; Schaeffer & Lebedev, 2013, 2014; Shapiro & Ritzwoller, 2002) of Greenland’s lithosphere have shown that the upper mantle can be broadly divided into two zones: a high seismic velocity region in the north-northwest and central western Greenland and a lower seismic velocity region to the south-southeast. A pronounced W-E trending upper-mantle low velocity corridor across central Greenland has also been resolved by various tomography models (Lebedev et al., 2017; Schaeffer & Lebedev, 2013, 2014). Other studies (Jakovlev et al., 2012; Rickers et al., 2013) show, however, very differently shaped corridors with substantial NW-SE offsets. Constraints on crustal velocity structure are limited, and general agreement on crustal structure remains a goal. Regional crustal shear wave tomography models from earthquake or ambient noise data suggest the presence of a low-velocity anomaly in northeastern and central eastern Greenland, but the amplitude and location of this anomaly differ between studies (Darbyshire et al., 2017; Levshin et al., 2017; Mordret, 2018).

The earlier work described above has provided valuable constraints on the properties of the crust and upper mantle underlying Greenland, which contribute to our understanding of the regional geologic history and help characterize the modern geologic environment. As with all regions, the accumulation of new data provides opportunity to continue to explore the region's subsurface building on earlier efforts. Recent evidences that parameters such as mantle temperature, viscosity, and lithospheric thickness, which affect surface heat flow and glacial isostatic adjustment, may influence ice sheet stability and glacier dynamics (e.g., Cuffey & Patterson, 2010; Larour et al., 2012; Pollard et al., 2005; Rogozhina et al., 2016; Stevens et al., 2016) provide impetus to continue our efforts to construct higher-resolution images of the subsurface beneath Greenland. For instance, a region of particular interest is the subsurface beneath the onset of the Northeast Greenland Ice Stream (NEGIS), which is unique among ice streams in that it originates far inland in a region of high GHF. Remotely resolving such small-scale features requires good images of the shallow and deep structure beneath the region. A decrease in seismic velocities in northeast Greenland, if observed, could be an indication of a potential thermal anomaly (e.g., Artemieva et al., 2004; Cammarano et al., 2003; Fullea et al., 2009; Goes et al., 2000; Priestley & McKenzie, 2006). But the fact that seismic velocities are sensitive to temperature, pressure, and composition adds to the interpretational complications. Resolving the differences remains a challenge, and the existence of unusual compositional variations in northeast Greenland cannot be eliminated.

In this study, we combine both ambient noise and earthquake data to investigate the lithospheric structure of Greenland with a focus on crustal structure. The high lateral resolution achieved by our earlier earthquake tomography (ET) maps (Pourpoint et al., 2018) and the increased bandwidth from the ambient noise allow constraints on the shear wave velocity structure as shallow as 10 km and down to 200 km. Model uncertainties are estimated from a Markov-Chain Monte Carlo (MCMC) sampling of the model space and are used to identify robust model features. We focus our discussion and interpretation on well-constrained features and attempt to address key questions in terms of the tectonic evolution of Greenland and how underlying geophysical processes may impact the ice stream dynamics and ice sheet stability.

2. Group Velocity Tomography

In this section, we briefly describe the procedures we used for processing earthquake and ambient noise data, along with the results, focusing on the results from the ambient noise tomography (ANT) which complement the ET results presented by Pourpoint et al. (2018). All the waveform data used in this study were obtained from the IRIS Data Management Center.

2.1. Earthquake Tomography

A detailed description of the processing and inversion of earthquake-based group velocities is presented in Pourpoint et al. (2018). A brief summary is provided here. We measured group velocities from seismograms generated by both regional and teleseismic earthquakes with a magnitude $M_w \geq 5$ and a focal depth $z \leq 100$ km that were recorded between 1994 and 2014 by the Greenland Ice Sheet Monitoring Network (GLISN; Clinton et al., 2014). GLISN is an international collaborative project with a goal of installing a permanent seismic and geodetic network in Greenland to provide data for multidisciplinary studies that monitor changes in the ice sheet dynamics and to characterize subglacial properties. GLISN includes 33 broadband seismic stations; of these, 4 are installed on the ice sheet and 15 are deployed on bedrock along the continental margins. The remaining stations are located in the Canadian Arctic, Iceland, Jan Mayen, and Svalbard. Most stations have been continuously recording data over at least 5 to 10 years. The stations used for ET are plotted as black and white triangles in Figure 2.

We used a multiple-filter analysis technique (e.g., Dziewonski et al., 1969) to estimate the group velocities of fundamental mode Rayleigh waves between periods of 25 and 170 s. To accurately resolve the structure within our region of interest, we incorporated corrections to account for the effects of heterogeneities in the structure outside of our study region (i.e., from the earthquake to the bounds of the study region). To do so, we used a group velocity correction based on the global dispersion model GDM52 (Ekström, 2011) to build path-specific dispersion curves. Despite a sparse network and limited local seismicity, this

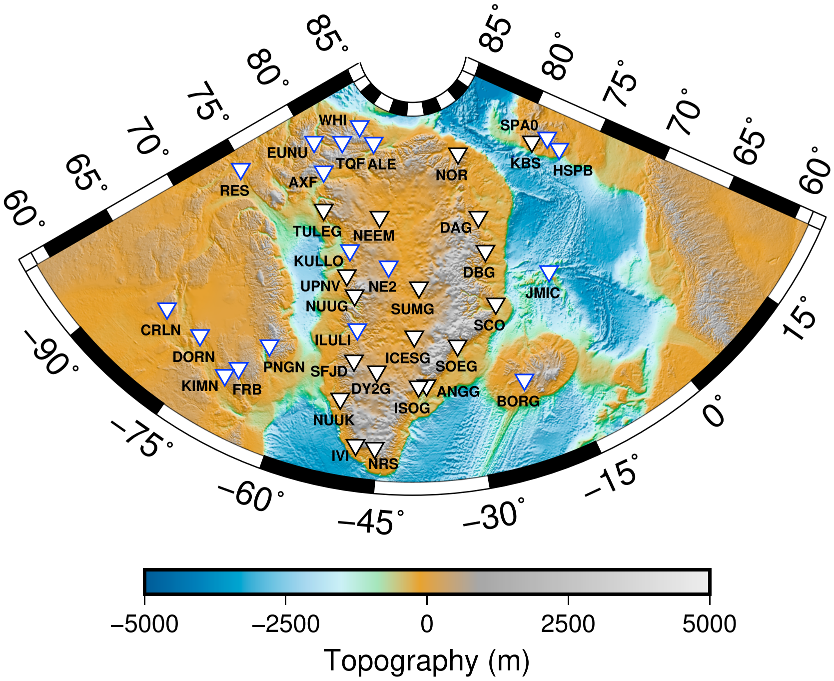

Figure 2. Map of the seismic stations used in this study. The stations used for earthquake tomography are plotted as triangles with black outlines. The triangles outlined in blue represent the additional stations used for ambient noise tomography. The stations are part of the Greenland Ice Sheet Monitoring Network (Clinton et al., 2014), and the XF (Nettles, 2014), X5 (Hudson Bay Lithospheric Experiment; Bastow et al., 2013), or 1E (Ellesmere Island Lithosphere Experiment; Stephenson et al., 2013) networks. The topography information is from ETOPO1 (Amante & Eakins, 2009).

technique allows us to improve the ray coverage and resolution of our study compared to studies using the two-station approach because it does not impose constraints on the array geometry and azimuthal distribution of events (Pourpoint et al., 2018).

To invert for ET dispersion maps, we discretized the model space using uniform velocity cells that are 111 km × 111 km (one-degree square). We used an iterative reweighted generalized least squares method to invert for the slowness in each cell. At each iteration, we reweighted the data with residuals larger than a fixed threshold by the inverse square of their residuals. Thus, data with large residuals were weighted less and more consistent observations weighted more in the model estimation. To stabilize this mixed-determined problem, we also applied a series of regularizations to the model perturbations. To find the best model that balances data misfit and model roughness, we performed a series of L-curve analyses (Aster et al., 2005) and assessed the model simplicity, lack of obvious artifacts, and resolution of known geologic features in choosing the preferred solution. We estimated the uncertainties in the dispersion maps by computing the root-mean-square (RMS) of the misfit between the observed and predicted group velocities at each period (Ritzwoller et al., 2001).

2.2. Ambient Noise Tomography

To build the ANT maps, we used the 33 GLISN stations along with eight additional broadband seismic stations: one from the XF network (Nettles, 2014), four from the Hudson Bay Lithospheric Experiment (X5 network; Bastow et al., 2013), and three from the Ellesmere Island Lithosphere Experiment (1E network; Stephenson et al., 2013). Stations used for the ANT are shown in Figure 2. Because of the relatively sparse seismic network across the study region and the two-station assumption required for measuring interstation ambient noise dispersion, strong constraints on crustal velocity variations from ANT are available only within Greenland, so we focus our MCMC inversion and analyses to Greenland.

We used continuous vertical component seismic data recorded from 2008 to 2016 and follow the approach described by Bensen et al. (2007) to retrieve the empirical Green's functions between station pairs. Since we use the vertical components only, the primary phases in the Green's functions are Rayleigh waves. The main processing steps include the following: segmentation of the continuous data into daily seismograms; preprocessing of the daily signal; normalization of the daily signal in the time domain to reduce the effects of transient signals like earthquakes, instrumental irregularities, and nonstationary noise sources; whitening of the daily signal over the frequency band of interest to flatten out the frequency content across all frequencies; cross correlation of daily signals between station pairs; and stacking to improve signal-to-noise ratio (SNR). These processing steps were performed using the MSNoise program (Lecocq et al., 2014).

Following Yang and Ritzwoller (2008), we estimate the characteristics of the ambient noise source based on the azimuthal distribution of the SNR of the stacked signals at all station pairs. For each station pair, we compute the SNR of the causal and acausal components of the stacked cross-correlation signal. Given a station pair A-B, if the SNR is stronger in the causal part of the signal (A→B), we assume that the energy is stronger at station A. Conversely, if the SNR is stronger in the acausal component (B→A), most of the energy is assumed to come from station B. The results of this analysis are presented as polar plots of the noise source distribution at each station and at discrete periods in Figure 3. At a given station, the direction from which the energy is coming is shown as a vector whose length is related to the SNR and whose direction is toward the location of the noise source. At short periods ($T \leq 10$ s), the strongest energy arrives from the north-northwest. Likely sources include oceanic gravity-wave interactions in the shallow water of Baffin Bay and along the north-northwestern margin of Greenland. At longer periods of 10 to 15 s, we observe a gradual shift in the noise source toward the north-northeast with more energy originating from the northeast margin of Greenland. At intermediate periods of 20 to 35 s, the noise sources are more diffuse with no obvious patterns in the energy propagation direction. The azimuthal range decreases at periods above 45 s, with stronger noise arriving from the northeast and possibly originating from interaction of oceanic waves in the deep water of the Greenland Sea and with the shallow coastlines of northeast Greenland.

We estimated group velocities for periods in the range from 8 to 65 s from the symmetric components using a multiple-filter analysis similar to that used for ET. We apply a series of quality control selection criteria including specifying a maximum period cutoff that depends on interstation spacing, a requirement that $SNR \geq 10$ at each period, and coherence across the measurements at each period. We obtained between 127 and 303 dispersion measurements per period (see Table 1). The ray coverage is best between periods of 10 and 40 s, decreasing at shorter and longer periods (Figure 4). Because of the station distribution, the coverage is also best in central western and central eastern Greenland, where we can resolve group velocity averages as small as 250 km. The results of the tomographic checkerboard and spike resolution tests (Barmin et al., 2001) are consistent with the ray coverage (Figure 4).

To invert for ANT dispersion variations, we again discretized the model space into 111-km × 111-km cells of uniform velocity and used an inversion scheme similar to that used for the ET. The derived group velocity maps (Figure 5) suggest significant variations in crustal velocity structure across Greenland. Relatively fast velocities are resolved in the south beneath the Archean cratonic block and along the Nagssugtoqidian fold belt and in the north beneath the Ellesmerian fold belt. A low-velocity anomaly is also observed beneath central Greenland at short periods ($T \leq 15$ s), extending toward northeastern Greenland at longer periods as Rayleigh wave group velocities sample the mid-to-lower crust. We discuss the significance of the results later, following the description of the inversion for shear wave velocity variations. As we did for the ET maps, we estimate the average uncertainty in the ANT maps using the RMS misfit from the tomographic inversion.

2.3. Localized Dispersion Curves From ANT and ET

Before merging the dispersion estimates, a direct comparison of the ANT and ET maps in the overlapping period band is valuable (Figure 6). Most velocity features are resolved by both ANT and ET, but differences are more pronounced in northern Greenland and at the southern tip where the ray coverage and resolution of the ANT are lower. The amplitude of the velocity variations is also smoother in the ANT maps. This discrepancy can be explained by differences in the smoothing applied for ANT and ET (i.e., greater smoothing is required to stabilize the ambient noise inversion) and could also be due in part to limited retrieval of empirical Green's functions at some station pairs from inhomogeneous distribution

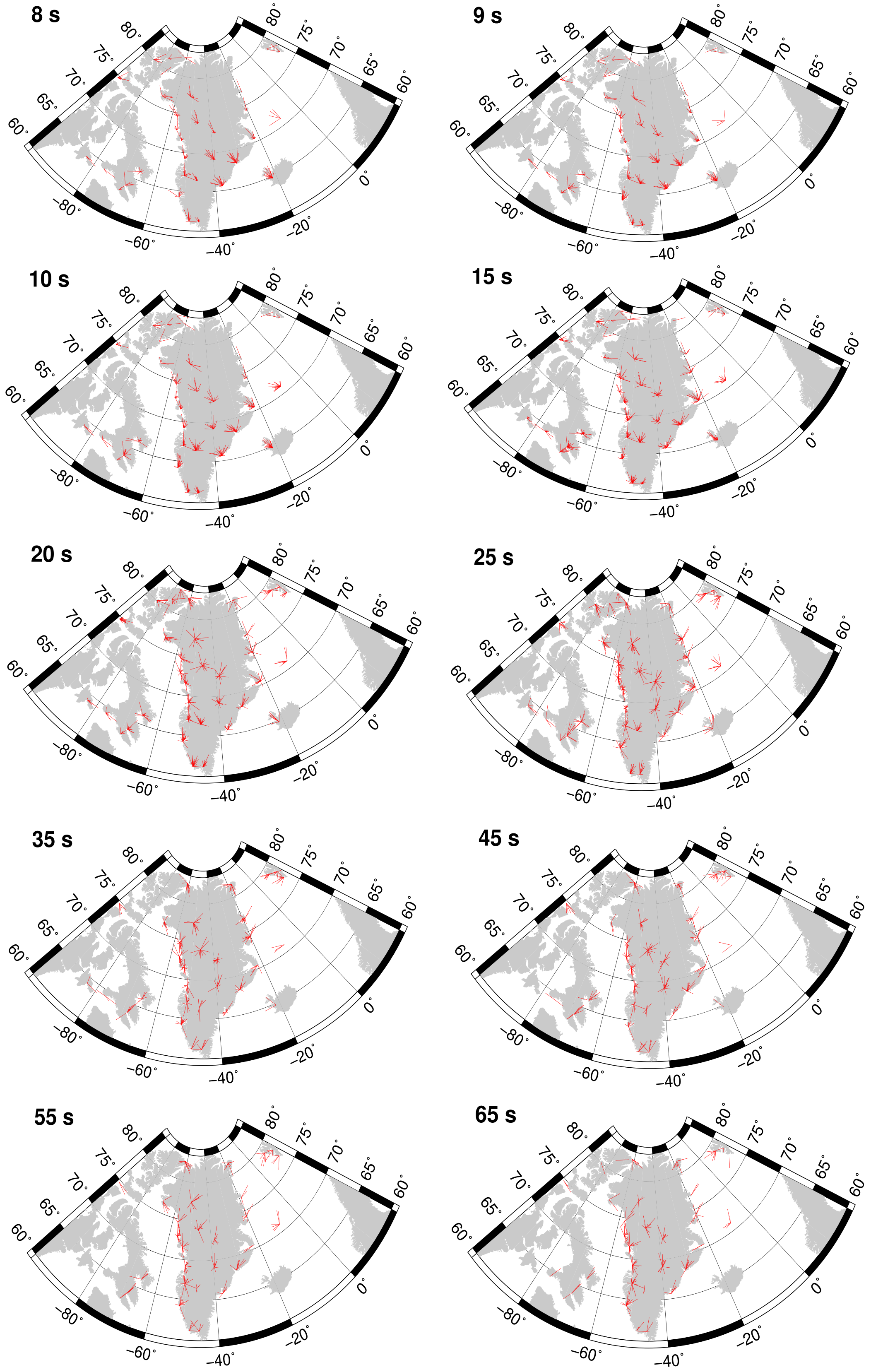

Figure 3. Map of azimuthal distribution of ambient noise measurement directions at discrete periods. At a given station, each vector (red line) points toward the location of the noise source. The length of each vector is signal-to-noise ratio dependent and normalized.

Table 1

Number of Ambient Noise Dispersion Measurements Rejected at Discrete Periods

	Period (s)													
Dispersion measurement	8	9	10	15	20	25	30	35	40	45	50	55	60	65
Total waveforms	590	590	590	590	590	590	590	590	590	590	590	590	590	590
FTAN discrepancy[a]	380	334	297	193	161	157	161	163	169	172	186	197	218	248
Interstation spacing[b]	0	0	0	5	9	14	21	35	35	39	40	43	41	36
$SNR < 10$	47	42	35	31	44	78	108	139	168	187	171	182	182	177
Visual inspection	12	11	24	61	63	43	31	22	9	2	2	2	2	2
Time residual[c]	2	7	9	9	10	6	6	2	1	2	2	3	0	0
Remaining measurements[d]	149	196	225	291	303	292	263	229	208	188	189	163	147	127

Note. SNR = signal-to-noise ratio.

[a] Frequency time analysis (FTAN) measurement failure corresponds to the number of nonmeasured dispersion points at a given period because of the discrepancies between the filter center period and the instantaneous period in the vicinity of a rapid change in the spectral amplitude of the signal. [b] At a given period, we reject any dispersion measurements with interstation spacing inferior to three wavelengths. [c] Following the inversion of a smooth initial group velocity model at each period, we reject any badly fitting dispersion measurements (i.e., any travel time measurements with a residual superior to three standard deviations of the travel time residuals). [d] Remaining dispersion measurements are used to derive the final ambient noise dispersion maps.

of noise sources (Yang & Ritzwoller, 2008). But the overall agreement between the independently derived dispersion maps confirms that the global correction approach is accurate enough to derive reliable regional tomography models.

To construct a broader bandwidth and a more robust data set, we combined the ANT and ET dispersion estimates. We selected group velocity measurements from ANT and ET for which the localized resolution is finer than 400 and 600 km, respectively. For periods shorter than 25 s, dispersion measurements are taken solely from ANT, and for periods ranging from 70 to 170 s, dispersion measurements are taken solely from the ET results. In the overlapping period band of 25 to 65 s, each localized dispersion curve is the average of the ambient noise and earthquake dispersions at the given cell, with the ambient noise measurements given greater weight at shorter periods ($T \leq 35$ s), and the earthquake measurements given greater weight at longer periods. Absolute differences between the ambient noise and earthquake-derived group velocities in the overlapping period band are typically in the range from 0.05 to 0.15 km/s. The discrepancies likely arise from a decrease in the SNR of empirical Green's functions at long periods ($T \geq 40$ s) and a decrease in the stability of the earthquake group velocity correction method at short periods ($T \leq 35$ s) but are within the estimated uncertainties in the dispersion measurements. Uncertainties in the combined, localized dispersion curves are taken from the ANT and ET tomography results. No smoothing is applied to the joint dispersion curves. Figure 7 illustrates the procedure, showing a localized dispersion curve and associated uncertainties as well as the original ANT and ET group velocity estimates. The consistency of the tomographic estimates is quite good.

3. Shear Wave Velocity Inversion

We followed a two-step approach to estimate the 3-D shear wave velocity structure of the lithosphere across our study region. We first inverted for a reference 1-D shear wave velocity profile in each cell using the iterative linearized least squares inversion method implemented in the Computer Programs in Seismology (Herrmann, 2013). We then performed a MCMC resampling (Mosegaard & Tarantola, 1995) localized in the region of model space surrounding the linearized solution to estimate uncertainties in the velocity model. We limit the application of this Bayesian approach to cells within Greenland because tomographic resolution decreases rapidly outside of Greenland.

3.1. Model Parameterization and Reference Model

The initial shear wave model is parameterized using estimates of the following: ice thickness from Bamber et al. (2001), sediment and crustal thickness and velocity and density from CRUST1.0 (Laske et al., 2013), and upper-mantle velocity and density from AK135 (Kennett et al., 1995). Estimates of anelastic attenuation for both the crust and upper mantle are taken from PREM (Dziewonski & Anderson, 1981). Topography and bathymetry are given by ETOPO1 (Amante & Eakins, 2009). Because Rayleigh waves are mostly sensitive to

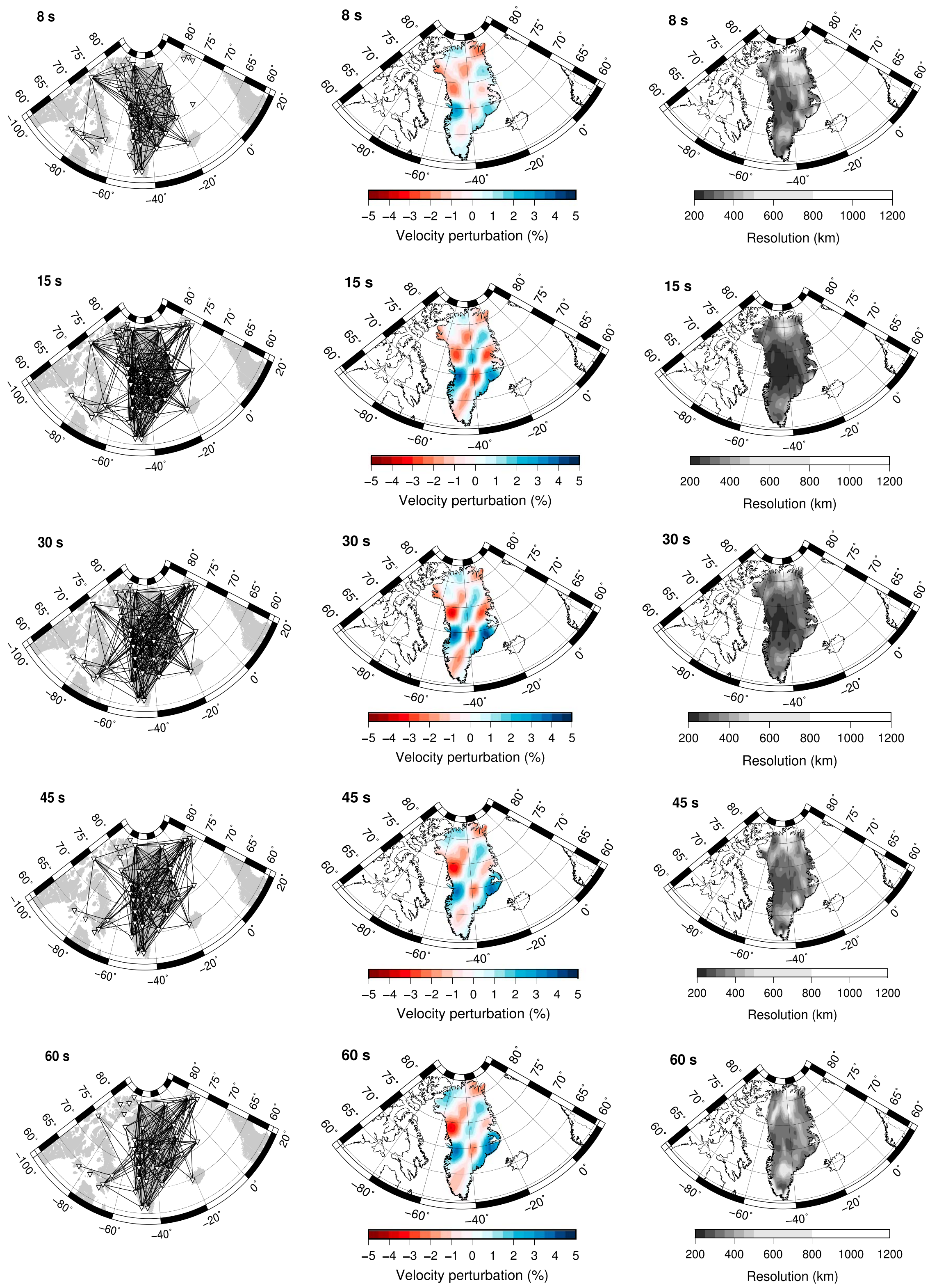

Figure 4. Maps of the ray coverage (left column), checkerboard resolution (middle column), and resolution length (right column) at increasing periods for the ambient noise tomography. The seismic stations used to derive the ambient noise tomography model are plotted as white triangles. For the checkerboard resolution tests, the input model has 444 km (latitude) by 555 km (longitude) checkerboard boxes. And, at each period, the starting model is given by the average of the estimated slowness model at this period with a ±5% slowness perturbation in alternating regions. Resolution length across Greenland is estimated following the spike-perturbation test of Barmin et al. (2001).

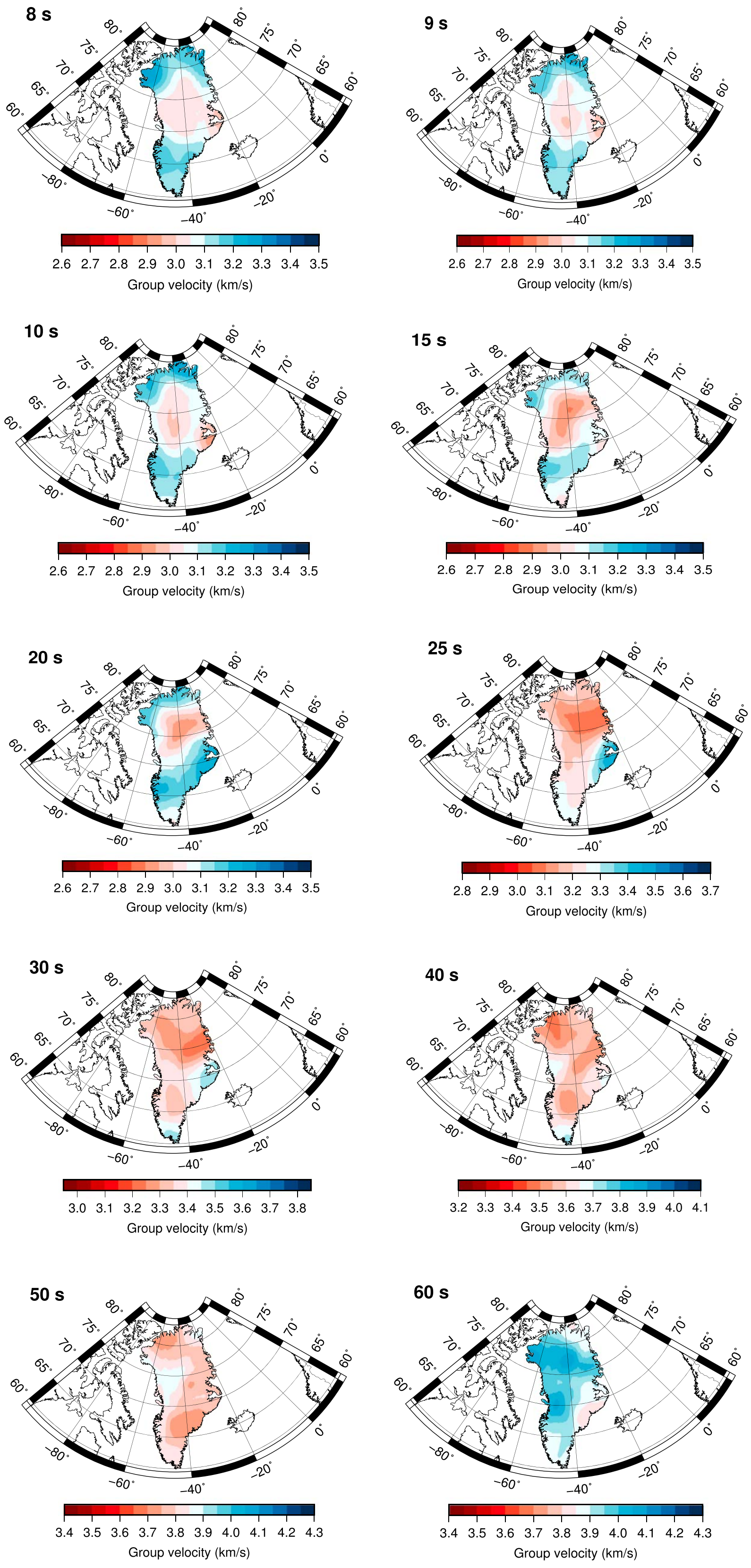

Figure 5. Rayleigh wave group velocity maps at increasing periods from ambient noise tomography. Velocity variations are plotted only across Greenland, where we have good ray coverage and resolution. Note the different velocity scales.

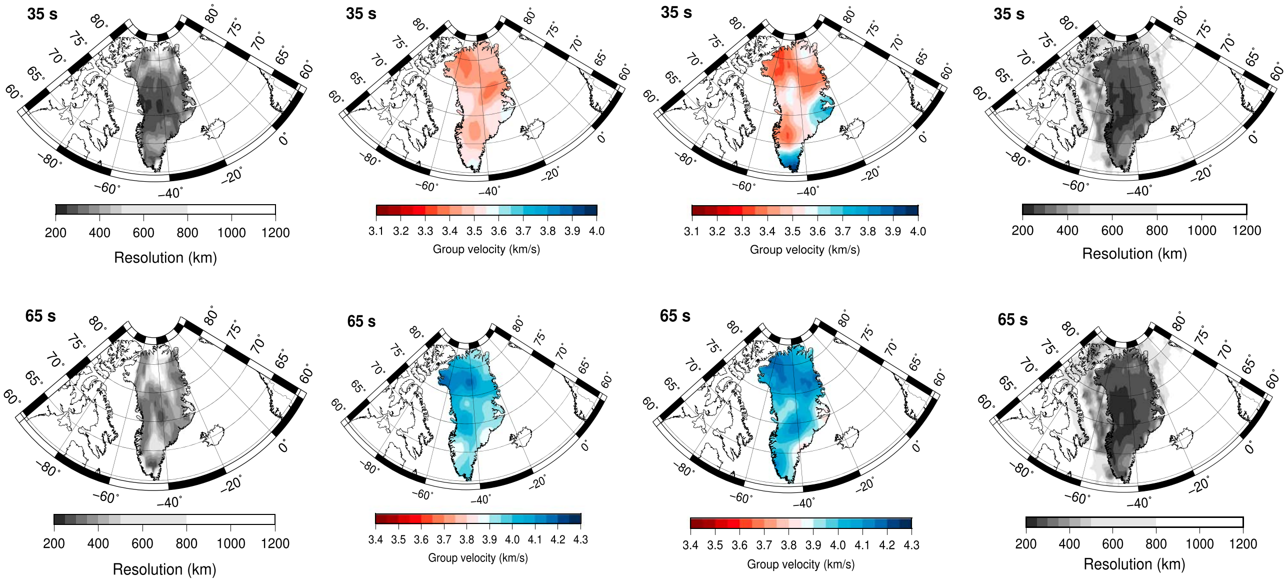

Figure 6. Comparison between the ambient noise tomography (second column) and earthquake tomography (third column) maps in the overlapped period band (25 to 65 s). Maps of resolution length from both ambient noise tomography (first column) and earthquake tomography (fourth column) are also plotted to explain some of the discrepancies between the two tomography maps.

vertically polarized shear wave velocities V_{sv}, we ultimately invert for the average 1-D V_{sv} structure beneath each cell, and we assume an isotropic structure. The thickness of each layer is fixed, and we use the empirical scaling relation from Brocher (2005) to estimate P wave velocity, V_p, as a function of S wave velocity, V_s, in the crystalline crust. We set the V_p/V_s ratio to 2.0 in the sedimentary layers and 1.79 in the upper mantle (Kennett et al., 1995). We estimate the density in the sedimentary layer, crust, and upper mantle from the polynomial regression fit of the Nafe-Drake curve (Brocher, 2005), which is a reasonable approximation. Since the fundamental mode Rayleigh wave sensitivity to variations in shear wave velocity decreases significantly below 200–250 km, the 1-D velocity models tie back to the global reference model AK135 below 250 km; however, we still invert for shear wave velocity down to 550-km depth, to avoid the smearing of deeper structures to shallower depths.

Once the reference 1-D models are estimated (see example in Figure 7), we simplify the parametrization for MCMC analysis by using a sedimentary layer, three crustal layers, and five cubic B-splines to represent the upper-mantle structure from the Moho discontinuity to a depth of 250 km. During the MCMC analysis, perturbations of both sediment layer thickness and velocity are allowed. The thickness ratio of the crustal layers is fixed at 1:2:2, but total crustal thickness and velocity in each crustal layer may vary. Given that model parameterization, the total number of free parameters is 11. The use of cubic B-splines imposes a degree of vertical smoothness and helps reduce the number of mantle depth parameters. The model parameterization and range of perturbations applied to the reference model are fixed across the region of focus and are summarized in Table 2.

3.2. Prior Distribution

Based on previous studies (Brocher, 2005; Dahl-Jensen, Larsen, et al. 2003; Kumar et al., 2007; Laske et al., 2013; Lebedev et al., 2017; Levshin et al., 2017; Shapiro & Ritzwoller, 2002), we limit the sampled model space to physically reasonable models, as summarized in Table 2. We apply the following a priori constraints to the parameter space: monotonic increase in velocity in the sedimentary and crustal layers, positive velocity contrast across the Moho discontinuity, and velocity and thickness perturbations within allowed ranges. These structural constraints help reduce model complexity and parameter trade-offs but also exert a significant influence on the prior and posterior model parameter distributions. The list of accepted models and the uncertainty estimates depend on the model parameterization and prior assumptions. First-order features should remain well resolved, but details must be assessed in light of the model parameterization, which limits the character of structures that we explore.

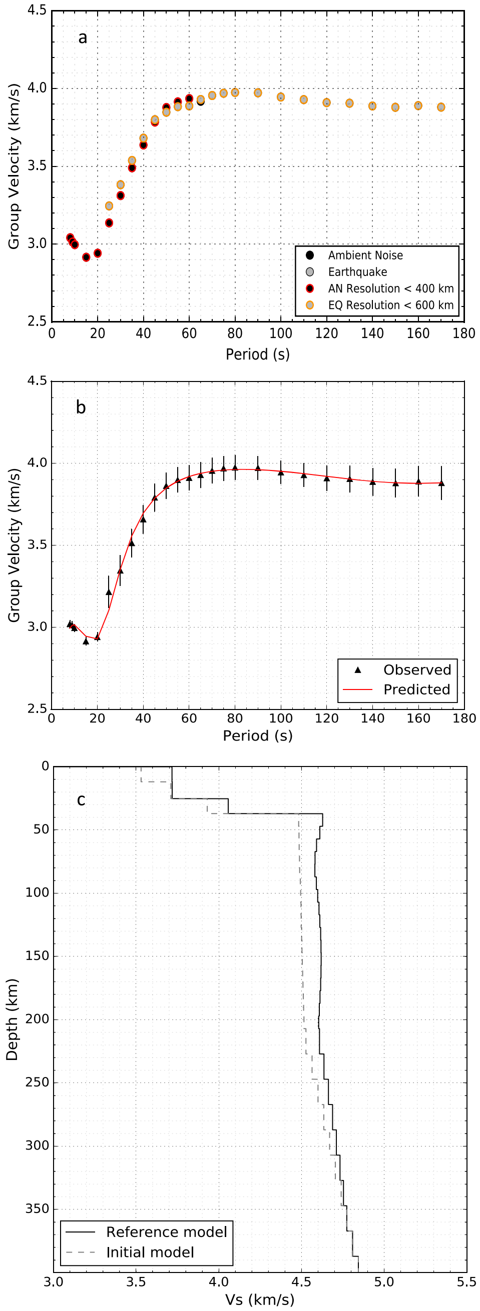

Figure 7. Localized group velocity dispersion curve (a, b) and derived 1-D reference shear wave velocity model (c) at a cell in central Greenland (location plotted in Figure 1). (a) The localized dispersion curves from ANT and ET are, respectively, plotted as black and gray circles. At a given period, a dispersion measurement is selected based on the localized resolution. Selected dispersion points are circled in red (ANT) or orange (ET). In this example, the ANT dispersion point at 65 s is shown but was not used in further analyses because of the lower localized ANT resolution. This plot shows the coherence between the two independent data sets. (b) The combined ANT and ET dispersion curve is plotted as black triangles and is referred as our observed dispersion curve. Uncertainties in the data are taken from the ANT and ET maps. The red curve is the predicted dispersion curve from the linearized inversion of the reference shear wave velocity model. (c) The 1-D initial and reference shear wave velocity profiles. ANT = ambient noise tomography; ET = earthquake tomography.

We build the prior distribution by uniform sampling of reasonably bounded model-parameter ranges (Table 2). We initiate the search at the simplified 1-D reference model and set up the random walk by introducing a random jump in the local space of plausible models. Model parameter jumps are controlled by a step size and maximum jump size specific to the parameter perturbed (Table 2). The step and maximum jump sizes, respectively, control how densely a model parameter is sampled and how much a parameter is allowed to change during an iteration of the search. The step and maximum jump sizes were tested to ensure that the model space is efficiently sampled and that local minima can be escaped. All 11 parameters were perturbed simultaneously to propose a new candidate model. If the proposed model exists in the plausible model space and satisfies the a priori model constraints, the model is accepted, and we reinitiate the uniform random walk at the most recently accepted model. We repeat this sampling process 20,000 times for each cell. The prior distributions of several sampled model parameters for a cell in central Greenland (74°N and 44.3°W; see Figure 1 for location) are presented in Figure 8. For each parameter sampled, the prior sampling of the model space is plotted as a histogram. In general, the prior distribution of V_s in the lower-crust layer tends to be more skewed toward its upper velocity limit because of limited constraints on crustal thickness and the resulting trade-offs between lower crust and upper most mantle velocities. Lack of constraints on the thickness of the sedimentary and crustal layers across Greenland is the direct result of limited a priori information on these parameters and limited sensitivity of surface wave dispersion to sharp velocity discontinuities.

3.3. Posterior Distribution

We assume a Gaussian distribution of uncertainties in the data and define the likelihood, L, as a function of the chi-square misfit, S, as follows:

$$L(m) = e^{-\frac{1}{2}S(m)} \quad \text{and} \quad S(m) = \sum_{i=1}^{N} \frac{\left(d_i^{\text{pre}}(m) - d_i^{\text{obs}}\right)^2}{{\sigma_i}^2}$$

where N is the number of periods at which we measure dispersion, d_i^{pre} is the predicted group velocity for model m at period i, d_i^{obs} is the observed group velocity at period i, and σ_i is the uncertainty in the observed dispersion, d_i^{obs}, at period i.

We use the Computer Programs in Seismology package (Herrmann, 2013) for the forward calculation of the predicted dispersion curves. To form the posterior distribution, we define the probability of acceptance of a proposed model according to the following Metropolis rule:

$$P_{\text{accept}} = \begin{cases} 1 & \text{if } L(m_p) \geq L(m_c) \\ L(m_p)/L(m_c) & \text{if } L(m_p) < L(m_c) \end{cases}$$

where m_c and m_p are, respectively, the current (i.e., previously accepted) and proposed models. That is, a proposed model is always accepted if its likelihood is greater than that of the previously accepted model and may still be accepted otherwise provided that its probability of acceptance is greater than a uniformly distributed random variable generated between 0 and 1. We always perturb the previously accepted model but keep a record of every proposed model and its associated misfit, to build our posterior distribution. Following the MCMC search,

Table 2
Model Parameters, Associated Ranges, Sampling Steps, and Maximum Jumps in Perturbation

Model parameters	Range	Sampling	Reference
Sediment thickness	$m_{\mathrm{ref}}{}^{a}$ ± 0.250 km	Step 0.01 km—Max jump 0.1 km	[1]
Vs sediment	$m_{\mathrm{ref}}{}^{a}$ ± 0.20m_{ref} (km/s)	Step 0.01 km/s—Max jump 0.05 km/s	[1] and [2]
Crustal thickness	$m_{\mathrm{ref}}{}^{a}$ ± 10 km (1:2:2 ratio)	Step 0.01 km—Max jump 0.1 km	[1], [3], and [4]
Vs crust #1	2.6–3.8 km/s	Step 0.01 km/s—Max jump 0.05 km/s	[1], [2], [5], and [6]
Vs crust #2	3.0–4.0 km/s	Step 0.01 km/s—Max jump 0.05 km/s	[1], [2], [5], and [6]
Vs crust #3	3.2–4.2 km/s	Step 0.01 km/s—Max jump 0.05 km/s	[1], [2], [5], and [6]
Vs mantle	4.0–4.9 km/s	Step ±5% coef$_{\mathrm{ra}}{}^{b}$—Max jump ± 10% $m_{\mathrm{ra}}{}^{c}$ (km/s)	[7]

Note. [1], Laske et al. (2013); [2], Brocher (2005); [3], Dahl-Jensen, Larsen, et al. (2003); [4], Kumar et al. (2007); [5], Levshin et al. (2017); [6], Lebedev et al. (2017); [7], Shapiro and Ritzwoller (2002).
[a] Reference model. [b] B-spline coefficients of most recently accepted model. [c] Most recently accepted model.

we introduce an additional localized acceptance criterion based on the minimum misfit for all proposed models at a given cell (Shen et al., 2012). We define this a posteriori criterion as follows:

$$\chi_{\mathrm{threshold}} = \begin{cases} (1 - \ln\chi_{\min})*\chi_{\min} & \text{if } \chi_{\min} < 0.5 \\ 0.5 + 0.7*\chi_{\min} & \text{if } \chi_{\min} \geq 0.5 \end{cases} \quad \text{and} \quad \chi = \sqrt{\frac{1}{N}*S(m)}$$

where χ is the variance-weighted RMS misfit for all proposed models. Any proposed model with a misfit smaller than that threshold is accepted. This criterion was defined to ensure that randomly rejected models that fit the observations within the data uncertainties are accepted and that the posterior distribution fully captures variations in the shear wave velocity model needed to fit the data.

3.4. Data Fit and Model Uncertainties

Results of the MCMC analysis show that the chosen model parameterization and a posteriori selection criterion allow us to effectively sample a posterior distribution of models that fit the data within the estimated

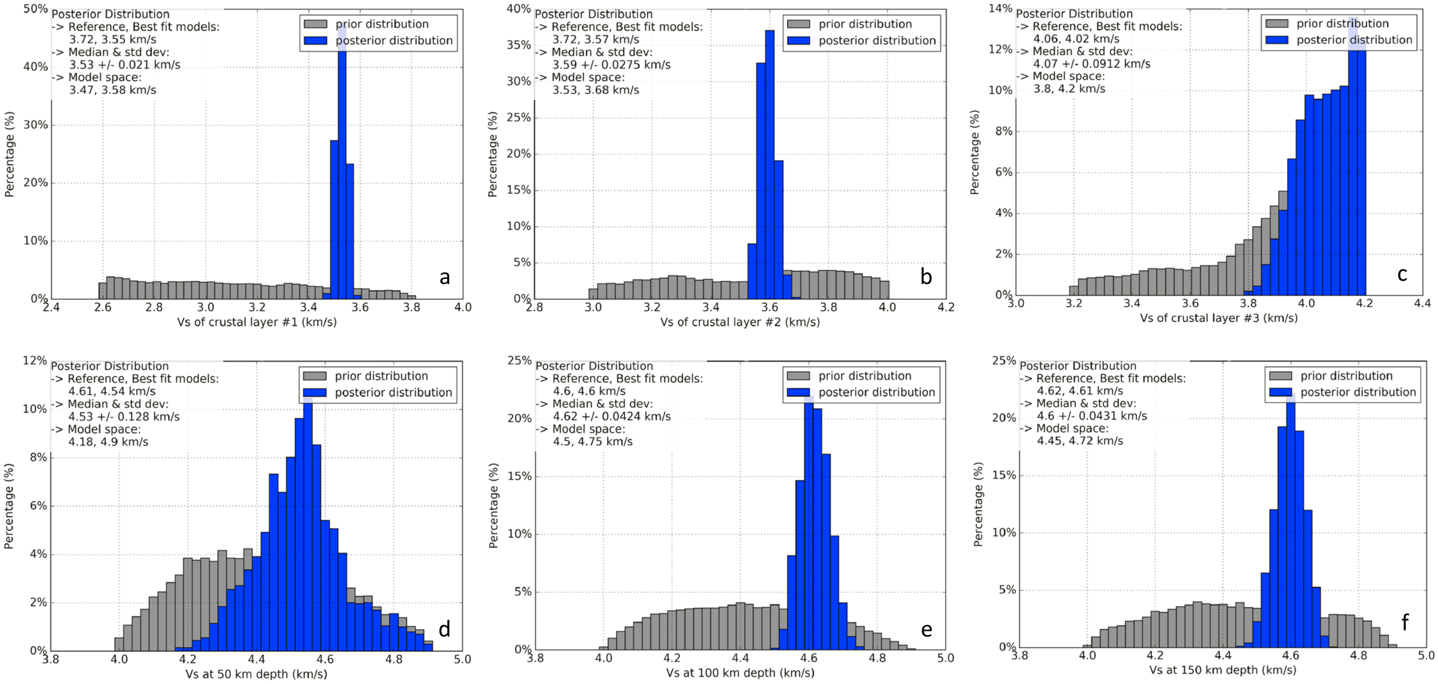

Figure 8. Prior and posterior distributions of several sampled model parameters at a cell in central Greenland (location plotted in Figure 1). The posterior distributions are plotted as blue histograms against their prior (gray histograms). In each panel, we specify the median and standard deviation of the posterior distribution as well as the reference model at which we start the Markov-Chain Monte Carlo search, the best fit model, and the range of accepted models. (a, b, c) Posterior and prior distribution of V_s in the upper, mid, and lower crust. (d, e, f) Posterior and prior distribution of V_s in the upper mantle at increasing depth (50 to 150 km).

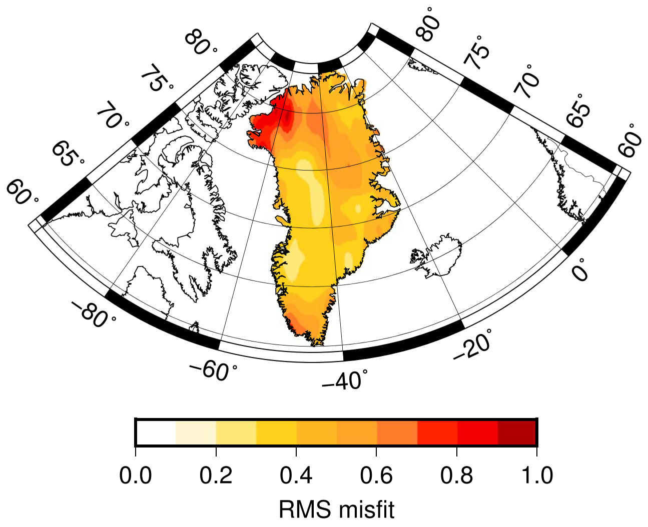

Figure 9. Map of RMS data misfit of the median models across Greenland.

uncertainties across most of Greenland. To identify a model representative of each distribution, we computed the median model (constructed using the median of each model parameter for all acceptable models). Since the problem is nonlinear, a median model is not guaranteed optimal in any way, but in our case, the models generally lie near the center of the model distributions at all depths and fit the observations as well as other acceptable models. As shown in Figure 9, the RMS misfit of the median models typically ranges from 0.2 to 0.6 (i.e., fit of the median models to the observations lies well within the data uncertainties). Cells for which the median model has a RMS misfit function as large as 1.0 are few and are mostly located in northwestern Greenland where we observe a relatively large data misfit (~25 to 75 m/s outside of data uncertainty range) at intermediate periods (80 to 110 s) and a shift in the distribution of uppermost mantle velocity toward the upper limit of the model space which may be a result of strong mantle anisotropy in that region (Pilidou et al., 2004). Short period ($T < 15$ s) data misfit is larger in regions with thick sedimentary basins (e.g., offshore western and northeastern Greenland), which suggests that the model parameterization should be changed in those regions; data fit could be improved by adding another sedimentary layer or considering a linear velocity gradient in the top layer.

An example of the posterior distribution of all accepted models for a cell in central Greenland is shown in Figure 10 (cell location in Figure 1). The accepted models and their fit to the observed dispersion curve are plotted as light gray curves (Figures 10a and 10b). Trade-off between model parameters and limited variability in the predicted dispersion curves suggests that a good fit is not a strong indicator of a robust velocity model. The nonuniqueness of well-fitting models is illustrated in Figures 10c and 10d. We use the median of the ensemble of acceptable models as our representative model (Figure 10a—red curve) and the standard deviation of all accepted models around the median model as our uncertainty estimate (Figure 10a—dark gray corridor). Histograms of the posterior distributions for a set of model parameters at the same cell are presented in Figure 8 and plotted with their prior distributions. Velocities in the upper and midcrustal layers (Figures 8a and 8b) are well constrained due to the addition of ambient noise data to the study, but the lack of short-period ($T < 8$ s) dispersion measurements prevents good resolution of sedimentary thickness and velocity. Trade-offs between lower crust and uppermost mantle velocity result in a more spread-out distribution of velocity across the discontinuity (Figures 8c and 8d). Long-period dispersion observations from earthquake data and a model parameterization that requires simplicity combine to produce relatively narrow distributions of the velocity in the upper mantle (Figures 8e and 8f).

Estimates of model uncertainty may be strongly influenced by the model parameterization. In a nonunique inversion, the greater the number of model parameters considered, the more complexity and trade-offs may be introduced and uncertainties may increase. Our model parameterization was chosen to identify simple models that match the data—our uncertainties are certainly conservative, and the models should only be interpreted in light of complementary geophysical and geologic information. Spatial variations in our estimated model uncertainties are summarized in Figures 11 and 12. In general, estimated uncertainties in V_s across Greenland are small and near uniform for the upper and midcrustal layers. The average uncertainty in these layers is roughly 30 m/s, which is almost certainly more optimistic than the true uncertainty. These are the layers covered by the short-period Airy phase and the initial trend of the strong intermediate-period gradient in dispersion. The data uncertainties at these periods ($T \leq 25$ s) are low (~20 to 30 m/s) and most likely underestimated leading to some underestimations of the uncertainties in V_s in the upper and midcrustal layers. Uncertainties increase with depth and are largest (~125 to 175 m/s) near the crust-mantle boundary depths where changing crustal thickness makes for a broad mix of crustal and mantle wave speeds. Large uncertainties in velocity near the Moho discontinuity are expected from the limited sensitivity of surface waves to velocity discontinuities; these uncertainties could be reduced by incorporating additional observations to the inversion (e.g., receiver function measurements and controlled-sourced imaging). Estimated uncertainties in the upper mantle are relatively small, roughly 60 m/s, as indicated by the sample probability density function in Figure 8. Parameterization again plays a role here; these numbers reflect the simplest

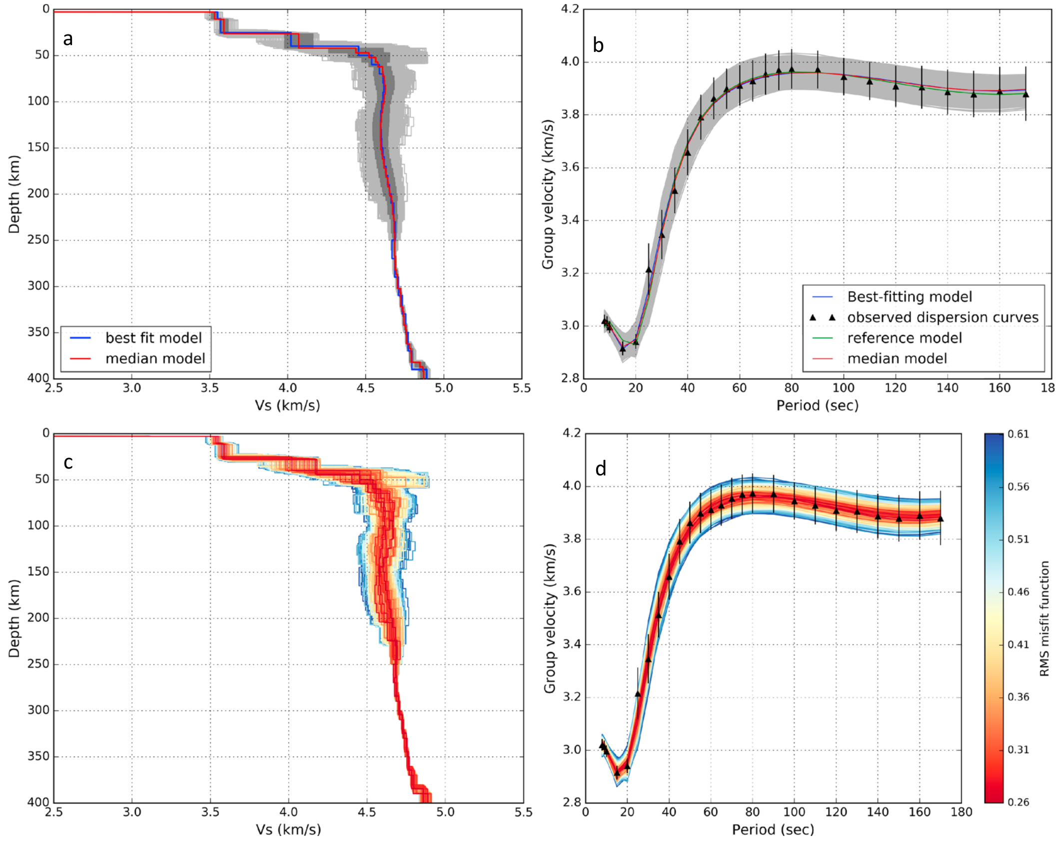

Figure 10. The model ensemble (a, c) at a cell in central Greenland (location plotted in Figure 1) and their fit to the observed dispersion curve (b, d). The light gray envelope in (a) and (b) shows the ensemble of accepted models and their predicted dispersion curves. The dark gray shaded area (a) represents the standard deviation of all accepted models around the median model (red curve in (a)). To highlight the nonuniqueness of the inversion and show that various V_S models can predict the data with the same level of fit, we color coded the ensemble of accepted models (c) and the modeled dispersion curves (d) based on their associated data misfit. The uncertainties in the observed dispersion curve are given by the RMS of the ANT and ET group velocity misfits as a function of period.

structures that match the observations. Some exceptions to the general trends are notable. At shallow depth (≤ 20 km), relatively large uncertainties along the northern and southern margins of Greenland are likely a result of a lack of short-period ($T < 25$ s) dispersion measurements in this region. Uncertainties in crustal thickness estimates are large, and the value at any single location is subject to at least ±5 km. Constraints on this depth range arise from the rapid increase in speed at periods from about 20–25 s to 40–60 s, which integrates contributions from the structure of entire crust and uppermost mantle.

4. Results and Discussion

We constructed a representative 3-D shear wave velocity model using the median of all acceptable models corresponding to each cell across Greenland and the 1-D reference models outside of Greenland. Each median model was checked to ensure that it fits the observations. Such approach can only resolve first-order features in the subsurface. Small variations in the median models are susceptible to variations in the initial model used in each cell's inversion, nuances associated with the model search sampling, nonlinear influences associated with the simple model parameterization, and the use of 1-D inversion results to construct a 3-D model.

Despite the large uncertainties, an interesting parameter in the model is crustal thickness. We estimate crustal thickness in each cell across Greenland as the sum of the thickness of the three crustal layers from the median model and define the depth to the crust-mantle boundary (Moho depth) as the crustal thickness minus topography (Figure 13). Since the range of crustal thickness is large, some general patterns are

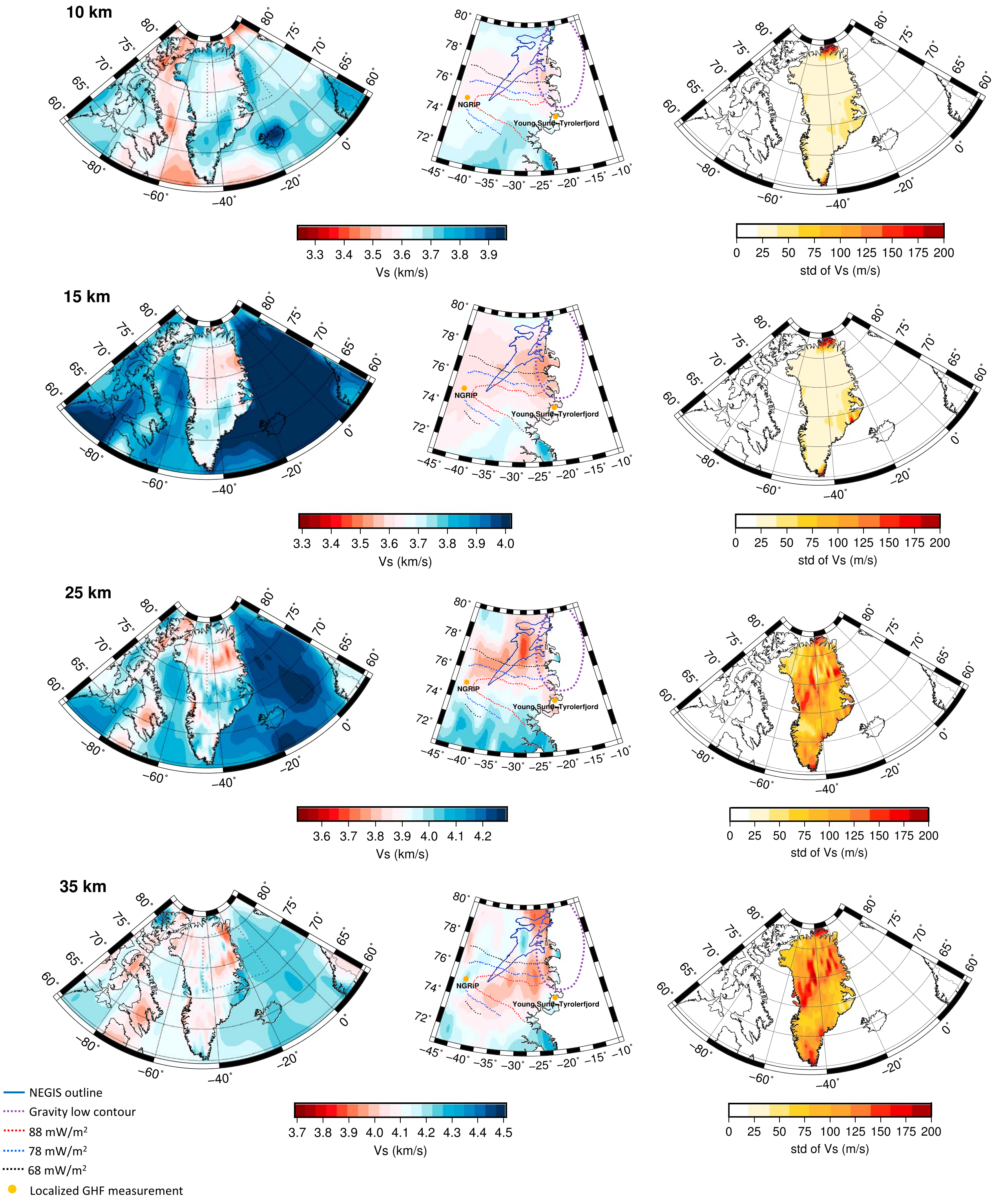

Figure 11. Crustal shear wave velocity model (left and middle columns, same color scale) and associated uncertainties (right column) at increasing depths. The middle column maps provide a zoom on the shear wave velocity variations across NE Greenland. The extent of this zoom is shown by the dotted black box on the left column velocity maps. In the middle column velocity maps, we plot the outline of NEGIS, contours of high GHF (after Rogozhina et al., 2016) and location of localized GHF measurements and gravity low (after Gradmann & Ebbing, 2015) to highlight that the ice stream is underlied by a shallow and relatively low velocity anomaly (NELVZ) and to point out spatial correlations between our study and previous geophysical studies. Uncertainty variations are only plotted across Greenland where we performed a MCMC resampling of the model space. NEGIS = Northeast Greenland Ice Stream; GHF = geothermal heat flux; NELVZ = northeastern low-velocity zone; MCMC = Markov-Chain Monte Carlo.

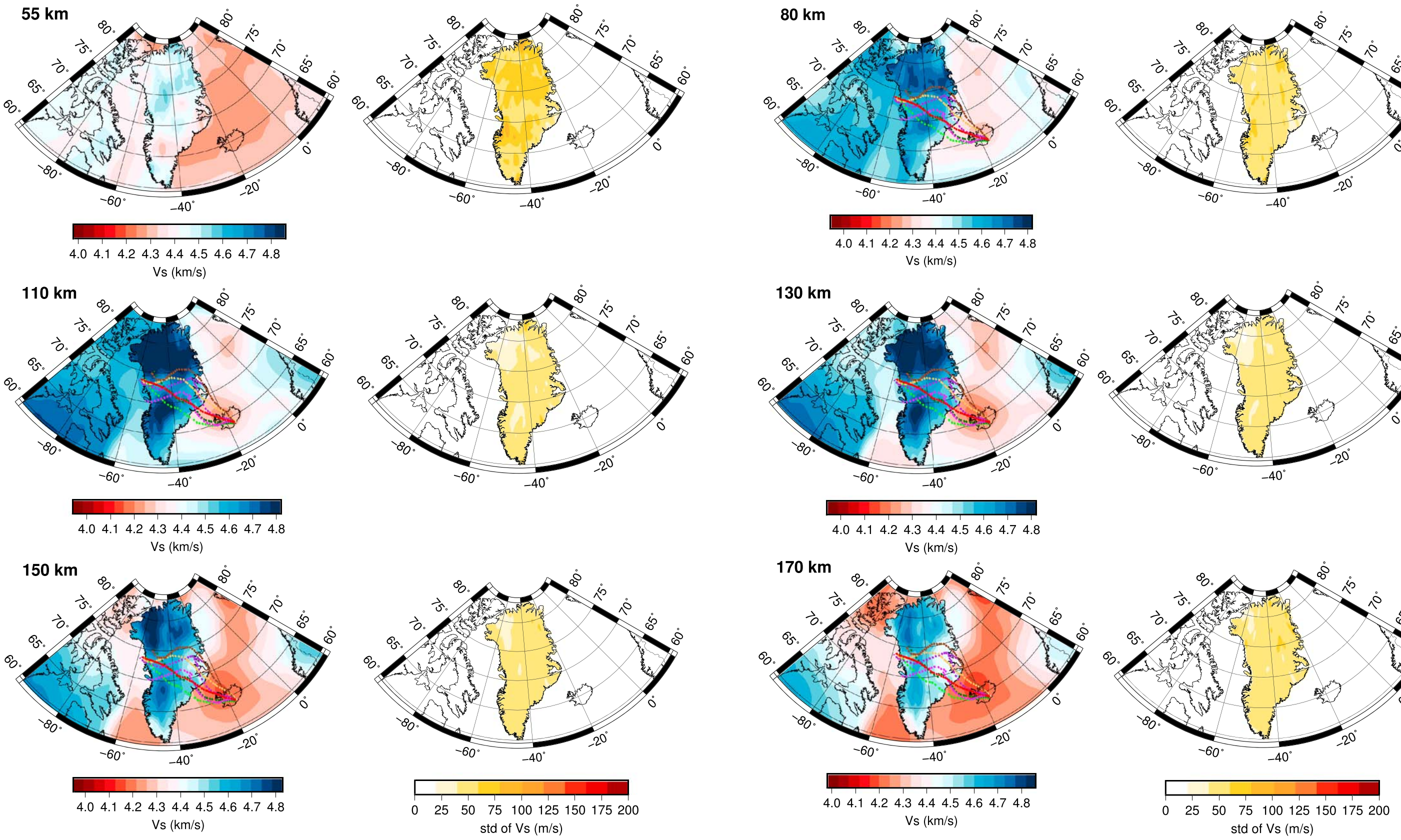

Figure 12. Upper mantle shear wave velocity model and associated uncertainties at increasing depths. We plot several predicted tracks of the Iceland plume relative to Greenland to show how they correlate with the W-E trending corridor of relatively low velocities across central Greenland. See Figure 1 for the full extent of these tracks as well as their color code. Uncertainty variations are only plotted across Greenland where we performed a Markov-Chain Monte Carlo resampling of the model space.

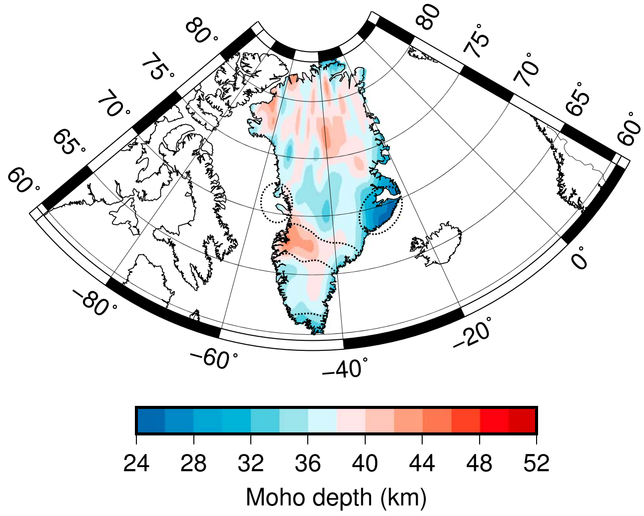

Figure 13. Map of Moho depth across Greenland. To point out correlations between Moho depth variations and tectonic provinces, we plot major terrane boundaries (dotted black lines). See Figure 1 for more details on the different tectonic units delineated by these boundaries.

worth noting. The results suggest thicker crust in the north, south central regions and thinner belt stretching east-west across central Greenland. The thinnest crust is along the central east margin. Still, we must consider potential trade-offs between uppermost mantle and lower crust and complexities not allowed in the inversion's model parameterization when interpreting our Moho depth model.

Horizontal slices of the composite 3-D velocity model are presented in Figures 11 (crust) and 12 (upper mantle) along with the estimated model uncertainties. In Figure 11, we overlay NE Greenland with GHF contours (Rogozhina et al., 2016; Rysgaard et al., 2018) to investigate a potential spatial correlation between regions of elevated heat flow, low gravity, and what we will refer to as a crustal northeast low-velocity zone. Vertical velocity transects across Greenland are also presented in Figure 14. The different regions, geological features, geophysical experiments, and velocity anomalies that are discussed below are located and labeled on Figures 1, 11, 12, and 14.

4.1. Lithospheric Structure

In this section, we present the main crustal and upper-mantle features imaged across Greenland and attempt to correlate our model with prior information on crustal thickness, margin segmentations, and

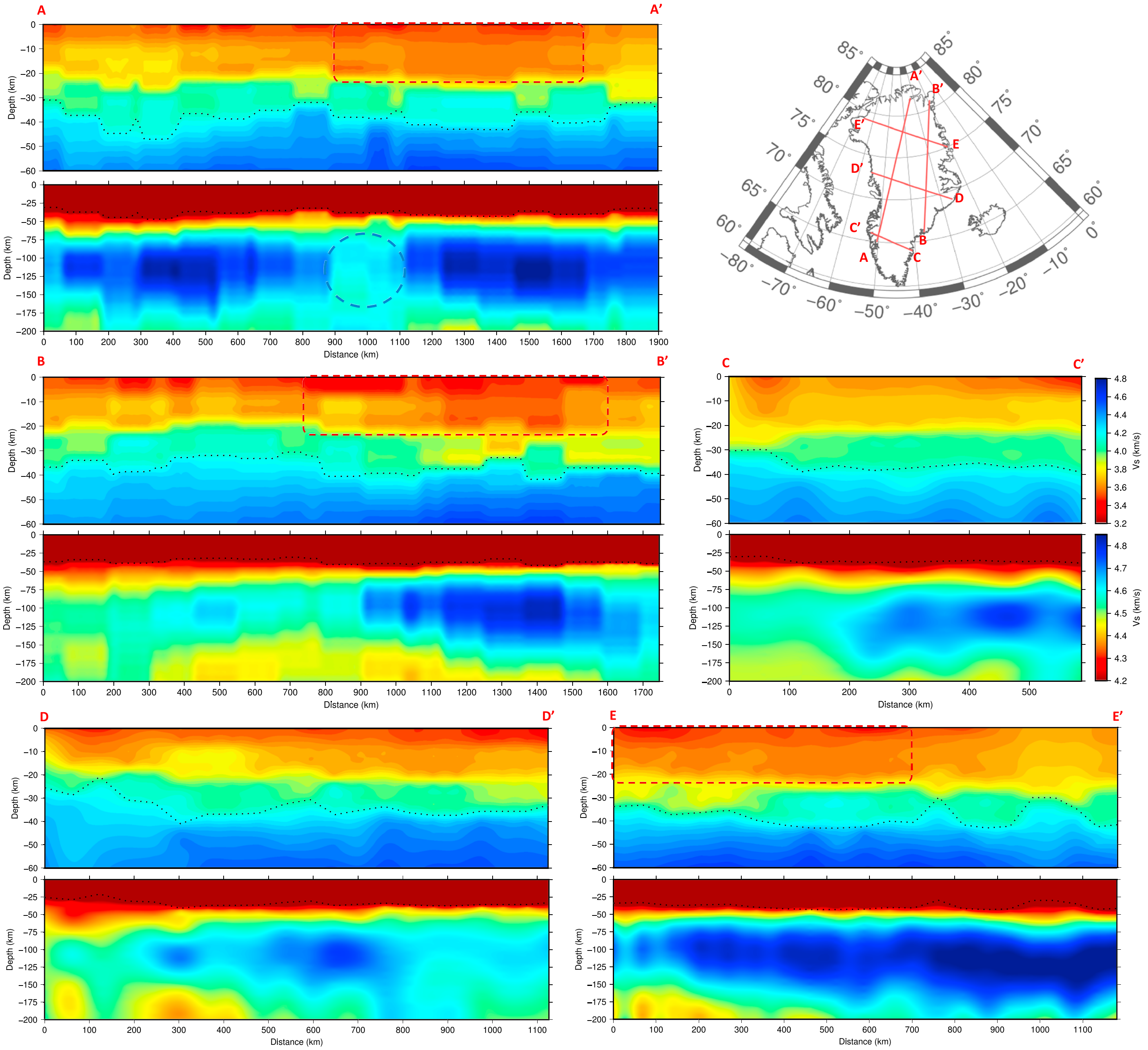

Figure 14. Cross sections through the velocity model for several profiles across Greenland. The location of the profiles is shown on the upper-right corner map. We present two panels per cross section, one focusing on the crust and uppermost mantle (top panel) and one presenting the whole velocity model (bottom panel). Note the different color scale used for each panel to emphasize small-scale velocity variations in both the crust and upper mantle. The color scales are the same for all cross sections. We contour the northeastern low-velocity zone (red dotted line—transects A-A′, B-B′, and E-E′) and the W-E trending upper mantle low-velocity corridor (blue dotted line—transect A-A′) to highlight their extent. The dotted black line marks the transition from crustal to upper-mantle velocity structure (Moho depth).

known terrane boundaries. Although we did not extend the MCMC search outside of Greenland, we also provide context for the large-scale features resolved by the reference models in the upper mantle.

4.1.1. Crustal Thickness Variations

Our representative 3-D shear wave velocity model of Greenland includes substantial variations in crustal thickness across Greenland, from roughly 25 to 45 km, with estimated uncertainties as large as 5 to 6 km

(Figure 13). This range is generally consistent with previous geophysical studies including surface wave tomography studies (Darbyshire et al., 2017; Mordret, 2018), receiver function analysis (Artemieva & Thybo, 2013; Dahl-Jensen et al., 2016; Dahl-Jensen, Larsen, et al., 2003; Kumar et al., 2007), and gravity studies (Braun et al., 2007; Petrov et al., 2016; Steffen et al., 2017). We describe regions where our crustal thickness estimates agree with other studies and present regions where our model significantly differs from other models and why that could be. But in light of our crustal thickness uncertainty, we focus only on first-order discrepancies (~10 km) we have with earlier estimates of crustal thickness.

Variations in the model crustal thickness correlate with some Precambrian terrane boundaries, notably in southern Greenland where the crust gets thicker as we transition from the Ketilidian Fold Belt to the South Archean Block. The thickest crust in our model is along the SW margin of Greenland (~67.5°N) where the collision between the South Archean Block and the Disko craton during the early Proterozoic produced the Nagssugtoqidian orogen (Ramberg, 1949; van Gool, Alsop, et al., 2002; van Gool, Connelly, et al., 2002). In this region, our model agrees well with crustal compilations such as CRUST1.0 (Laske et al., 2013) and receiver function studies (Artemieva & Thybo, 2013; Dahl-Jensen et al., 2016; Dahl-Jensen, Larsen, et al., 2003; Kumar et al., 2007). Gravity results from Petrov et al. (2016) and surface wave tomography results from Mordret (2018) also suggest thickened crust in this region. From this region, relatively thick crust extends southward and eastward and coincides with part of the South Archean Block, Eastern Archean Block, and Nagssugtoqidian orogen. In northern Greenland, our model does not indicate crustal thinning as suggested by gravity-based models (Braun et al., 2007; Petrov et al., 2016; Schiffer et al., 2018; Steffen et al., 2017) but is relatively consistent with surface wave-based crustal thickness models (Darbyshire et al., 2017; Mordret, 2018). The high degree of heterogeneity in crustal thickness estimates in northern Greenland may be the result of the limited sensitivity of surface waves. But differences between the northern and the central/southern parts of Greenland could also suggest greater crustal complexity in northern Greenland than in the south.

Compatibility between our model and more localized thickness estimates is variable along the continental margins. Crustal thickness variations along the SW and SE margins are in relatively good agreement with seismic refraction and reflection profiles that estimate thickness ranging from ~30 km in the southwest (Chian & Louden, 1992) to 30–35 km in the southeast (Funck et al., 2017; Hopper et al., 2003; Korenaga et al., 2000). Our model is also in relatively good agreement with the receiver function estimates of Schiffer et al. (2015) in the Central Fjord Region of East Greenland (73°N) where crustal thickness is thought to increase from ~25 km (22°W) to ~40 km (29°W) toward the center of the Caledonian high topography. Similar crustal thickness variations are also found in this region along different active source profiles including the lines AWI-94360 and AWI-94320 (Schmidt-Aursch & Jokat, 2005) and the line AWI 20030400 (Voss & Jokat, 2007).

In central eastern Greenland south of the 72°N lineament, our model suggests significant crustal thinning, which is inconsistent with results of seismic profiles to the order of 10 km (line AWI 94320—Schlindwein & Jokat, 1999; line SIGMA 1—Holbrook et al., 2001; and lines AWI-90300/310, AWI-94400, AWI-90380, and AWI-94410—Schmidt-Aursch & Jokat, 2005). The lack of a pronounced Caledonian crustal root south of 72°N in our model is also inconsistent with gravity-based models (Braun et al., 2007; Petrov et al., 2016; Steffen et al., 2017) but is overall in better agreement with receiver function studies (Artemieva & Thybo, 2013; Dahl-Jensen, Larsen et al., 2003; Kumar et al., 2007) and the recent surface wave study of Darbyshire et al. (2017). The discrepancy between our crustal thickness estimates and the active seismic profiles could be attributed to the presence of high-velocity lower crustal (HVLC) layers from magmatic underplatting during continental breakup and the later passage of the Iceland plume beneath CE Greenland (Hermann & Jokat, 2016; Holbrook et al., 2001; Schiffer et al., 2015). The presence of these magmatic accretions could complicate the crust to mantle transition and bias our model results. But it is worth noting that the possible presence of HVLC layers south of 72°N is still a matter of debate (Schlindwein & Jokat, 1999; Schmidt-Aursch & Jokat, 2005). Discrepancies between the gravity models and our thickness estimates could reflect differences between seismic and isostatical Mohos as they are indicative of different subsurface property discontinuities. On the other hand, thin crust in CE Greenland (our model; Artemieva & Thybo, 2013; Dahl-Jensen, Larsen et al., 2003; Darbyshire et al., 2017; Kumar et al., 2007; Laske et al., 2013) could be the result of extensive stretching of continental crust during rifting and spreading of the North Atlantic Ocean and may also reflect interactions of the North Atlantic rifting with the Iceland plume ~56 to 35 Ma.

4.1.2. Velocities in the Crust

We begin with a Greenland-wide discussion, then focus on velocity features along the continental margins, and conclude with an exploration of the model characteristics in northeast Greenland, an area of special interest given previous estimates of relatively high heat flow in a region of rapid ice flow (Figure 11). In the depth range from 10 to 25 km, the velocity model includes a roughly 0.15–0.25 km/s velocity increase from the north to the south, where average crustal velocities are more consistent with other cratonic shields (Chen et al., 2015; Christensen & Mooney, 1995; Kao et al., 2013; Gu & Shen, 2015; Yuan, 2015). In the 10- to 15-km depth range, the model suggests a SW-NE trend to the velocity transition. Geographically, the transition roughly separates the Nagssugtoqidian and Rinkian orogens in western Greenland and trends northeastward to a region north of the Kong Oscar Fjord (~73°N). A likely tectonic and structural boundary has been previously identified in western (van Gool, Connelly, et al., 2002; Wardle et al., 2000) and eastern Greenland (Brooks, 2011; Escher & Pulvertaft, 1995; Hamann et al., 2005; Henriksen et al., 2008, 2009; Koch & Haller, 1971; Larsen, 1990) where the crystalline crust is composed primarily of Archean and reworked Archean rocks to the south of this boundary and Paleoproterozoic rocks to the north. The importance of this boundary on the eastern margin is also suggested by persistent differences in geological evolution, including in late Paleozoic and Mesozoic rift basin formation and sediment deposition (Henriksen et al., 2008; Stemmerik et al., 2013; Surlyk, 1990; Tsikalas et al., 2005) and in styles of magmatic emplacement (Funck et al., 2017; Schlindwein & Jokat, 1999; Schmidt-Aursch & Jokat, 2005). A similar SW-NE boundary separating regions of different crustal thickness has also been inferred from receiver function and gravity studies (Dahl-Jensen, Larsen, et al., 2003; Petrov et al., 2016; Steffen et al., 2017). The velocity transition is absent in the 35-km depth slice where our model uncertainty increases substantially because of resolution issues described earlier.

Our model includes heterogeneity in crustal structure along the margins of Greenland. Between roughly 66 and 70°N and from 10- to 20-km depth, a succession of relatively high velocity zones in our model appears to follow the transition from the southern, central, and northern tectonic segments of the Nagssugtoqidian orogen (van Gool, Alsop, et al., 2002; van Gool, Connelly, et al., 2002). The orientation of this succession of high velocity zones is also similar to the WSW-ENE trending linear belt characteristics of the Nagssugtoqidian orogen. In southernmost Greenland, between roughly 60.5 and 62°N and from 10- to 30-km depth, our crustal velocities are consistent with the seismic refraction model of Chian and Louden (1992) who imaged the crust along the SW boundary separating the South Archean block and the Ketilidian fold belt. The boundary between the two terranes is marked by relatively low crustal velocities within the Ketilidian fold belt. Our model does not include HVLC layers under the western margin of the Ketilidian fold belt, which is in good agreement with a study by Keen et al. (2012) suggesting that the SW Greenland margin transitions from a volcanic to a nonvolcanic margin at about 62°N (from north to south; see also Alsulami et al., 2015). The associated changes in crustal properties (from magma rich in the north to magma poor in the south) could also explain the gradual decrease in velocity that we observe between 10 and 30 km along the southwestern margin of the South Archean block (from north to south). Along the southern tip of the Ketilidian fold belt, the transition from nonvolcanic margin and relatively thin crust (~30 km) to the SW to volcanic margin and relatively thick crust (~35 km) to the SE (Larsen, 1990) may be reflected by the model transition from relatively fast to relatively slow from west to east at 35-km depth. This velocity pattern agrees with evidence of underplated material beneath the SE Greenland margin from magma accumulation during Tertiary rifting of the North Atlantic (Dahl-Jensen et al., 1998). In CE Greenland, between 20- and 35-km depth, we find velocities as high as 4.1 to 4.3 km/s that could indicate magmatic underplating of the lower crust or relatively thin crust in this region. As outlined in the previous section, general disagreement in crustal thickness estimates in CE Greenland and the increasing trade-off between Moho depth and lower crustal velocity in this depth range in our model make it difficult to favor a particular scenario.

An intriguing feature in the velocity model is the relatively low velocities imaged in NE Greenland and hereinafter referred to as the northeastern low-velocity zone (NELVZ). The feature (Figure 11—middle column) becomes more anomalous and spreads out at midcrustal depths (15 to 25 km). Potential trade-off between crustal thickness and lower crustal velocity, however, prevents any clear estimates of the extent of this anomaly below 20- to 25-km depth. This limitation is illustrated (Figure 11—25- and 35-km horizontal transects) by relatively high uncertainties in velocity in NE Greenland. Darbyshire et al. (2017) also imaged a relatively low velocity anomaly in NE Greenland with more spatial variability. The differences likely result from the significant differences in short-period dispersion estimates ($T \leq 20$ s), which arise from the different data sets used at short periods (i.e., ambient noise in this study vs. earthquake data in their study). We believe that the ambient noise provides more accurate information on the shortest period dispersion. But the spatial extent and position of our NELVZ differs somewhat from the location of a similar anomaly estimated in a recent ANT study by Levshin et al. (2017). In that study, the low-velocity anomaly is more centrally located and of smaller magnitude. The location of the NELVZ is in better agreement with the ANT model of Mordret (2018) at 10-km depth, but discrepancies in magnitude and in the spatial extent of the anomaly at 25-km depth exist. The low-velocity anomaly imaged in that study is reduced in amplitude and more spread out in the mid-to-lower crust. Although more work is required to resolve these differences, we proceed with an assumption that our study using ambient noise and earthquake data (a broader bandwidth) provides an accurate view of the region. A first-order explanation of the NELVZ would be to attribute the relatively low crustal velocities to a local increase in crustal thickness in NE Greenland. Crustal thickness may change in the region, but at least the upper half of the low-velocity anomaly is too shallow to be a result of variations in crustal thickness alone. An intriguing possibility is that the NELVZ is the signature of a thermal or compositional heterogeneity. We explore this idea and the correlation of this feature with other geophysical anomalies in NE Greenland in section 4.2.

4.1.3. Velocities in the Upper Mantle

Our model (Figure 12) suggests that a cratonic keel extends from SW to NW-NE Greenland that is separated by a corridor of relatively low velocity across central Greenland. This low-velocity feature is consistent with the upper-mantle model of Lebedev et al. (2017) but not present in the model of Darbyshire et al. (2017). However, the latter model only extends to a depth of 90 km and has limited ray coverage and resolution at these depths. A similar feature is contained in the global models SL2013sv and SV2013NA of Schaeffer and Lebedev (2013, 2014) and the regional model of Mordret (2018). This low-velocity corridor is especially interesting because it appears to connect the western and eastern Tertiary basalt provinces. The feature is about 200 km wide and includes a relative velocity reduction in the range of 3% to 6% (Figure 14—Transect A-A′). Two leading explanations for this feature are a tectonic boundary or long-lived effects of the passage of the Iceland plume beneath Greenland. The low-velocity corridor could be the signature of a tectonic boundary between two cratonic blocks as it more or less aligns with the surface geological boundary and upper-crustal velocity contrast described earlier (Lekic & Romanowicz, 2011; Schaeffer & Lebedev, 2014). Alternatively, this anomaly could indicate lithospheric modification or delamination related to the passage of the Iceland plume beneath Greenland. Uncertainties in paleoreconstructions of the Iceland plume track beneath Greenland are large and increase the further we get from the current location of the Iceland hotspot (Figure 1—right column; also see Rogozhina et al., 2016). But the low-velocity corridor matches several of the proposed plume tracks. The two potential explanations are not mutually exclusive. From Sleep (1997), buoyant plume material preferentially flows toward regions of thinner lithosphere. Thus, thermal erosion and thinning of the cratonic lithosphere from the Iceland plume may have focused in preexisting zones of lithospheric weakness, leaving the high-velocity cratonic keels in NW-NE and SW Greenland relatively unaltered (Sleep et al., 2002).

Below ~150 km, relatively low velocity anomalies are observed in CE and southern Greenland (Figures 12 and 14—transects C-C′ and D-D′). The CE low-velocity anomaly underlies the eastern Tertiary Basalt Province and is most likely associated with lithospheric thinning from upwelling of asthenosphere material during the rifting of the North Atlantic Ocean and subsequent passage of the Iceland mantle plume beneath CE Greenland, with plume interactions continuing to ~5 Ma or more recently (Japsen et al., 2014; Schoonman et al., 2017; Steinberger et al., 2015). Present-day upwelling, if originating from the lower mantle, would probably have a signature in the mantle transition zone (i.e., reduced width; see Kraft et al., 2018). Thin lithosphere in central eastern Greenland could, alternatively, further delineate the extent of a possible tectonic boundary between north and south cratonic blocks. In both cases and independent of potential temperature, thin lithosphere would cause elevated GHF in the region (e.g., Rogozhina et al., 2016; Rysgaard et al., 2018). The low-velocity anomalies from CE Greenland are consistent with previous *P* and *S* waves tomography (Jakovlev et al., 2012; Lebedev et al., 2017; Mordret, 2018; Rickers et al., 2013; Schaeffer & Lebedev, 2013, 2014) and with indications of lithospheric thinning in this region (Kumar et al., 2005; Schiffer et al., 2018). The presence of this mantle low-velocity anomaly in a region of documented postrift uplift (Anell et al., 2009; Døssing et al., 2016; Japsen & Chalmers, 2000) and unusually high GIA uplift rates (e.g., +10 mm/year; Khan et al., 2016) could also be an evidence of low upper mantle viscosity and explain the mechanism for isostatic compensation in a region with no deep crustal roots. The lack of a similar velocity low beneath the western Tertiary Basalt Province in this depth range could indicate limited lithospheric modifications from the failed rifting of the Labrador Sea. In southern Greenland, low upper mantle velocity could also be attributed to lithospheric thinning during rifting of the Labrador Sea and North Atlantic Ocean and subsequent continental breakup of North America from Europe during the late Cretaceous to early Tertiary.

In the upper mantle, low velocities are also imaged along the Mid-Atlantic ridge, with anomalies centered beneath Iceland and the Knipovich Ridge. Both anomalies are clearly resolved and distinguishable from 80- to 170-km depth, but the Knipovich Ridge anomaly becomes stronger and more elongated with increasing depth ($\geq$130 km), extending toward Svalbard. The elongated aspect of this low-velocity zone along the North Atlantic mid-oceanic ridge has been imaged by most tomography models and is characteristic of the modeled plume-ridge interaction from channeled flow of plume material along the ridge (Pilidou et al., 2004). A gradual increase in velocity with increasing distance from the Mid-Atlantic ridge is also resolved and is consistent with cooling and thickening of oceanic lithosphere away from the ridge. At depths of 110 to 130 km, our model reveals a low-velocity finger extending from the Iceland hotspot to southern Scandinavia; similar anomalies have been previously imaged (Rickers et al., 2013) and modeled (Schoonman et al., 2017). The high-velocity lids beneath the Canadian and Baltic Shields are clearly visible to ~150- to 170-km depth, but the limited resolution of our model in these regions prevents accurate estimates of lithospheric thickness. At 110 km and deeper, a well-defined boundary separates the Canadian and Greenland shields, with seismic velocity transitioning from relatively fast beneath the thick cratonic lithospheres to relatively slow beneath the tectonically younger Labrador Sea and Baffin Bay. The velocity heterogeneity across the Labrador Sea and Baffin Bay may suggest lateral variations in lithospheric thickness, with thicker oceanic lithosphere to the north of the Davis Strait. These variations are consistent with regional tomography models (Lebedev et al., 2017; Schaeffer & Lebedev, 2014) and the lithosphere-asthenosphere boundary depth model of Schiffer et al. (2018).

4.2. Northeast Greenland Low-Velocity Anomaly

Given the fact that the NELVZ underlies NEGIS, which drains more than 20% of the Greenland Ice Sheet (GIS; Zwally et al., 2012), and that the potential source of the low velocities could impact the ice stream dynamics and the ice sheet evolution, we spend the remainder of the discussion focusing on the origin and significance of the NELVZ (Figure 11—mid column). We emphasize that the NELVZ is an anomaly with respect to typical crustal velocity for stable cratonic regions and that our velocity model precludes any ongoing and widespread partial melt in NE Greenland. But in light of previous evidences of elevated GHF, high basal melting rate and gravity low in the region, it is worth further exploring the nature of this velocity anomaly. We start this section with a review of relevant literature and how the NELVZ correlates with the results of those studies. We then integrate the evidence to develop a coherent and geologically plausible scenario for the emplacement of the NELVZ.

A prominent gravity low (i.e., 500 × 200 km large and 100 mGal in magnitude) has been identified along the northeastern margin of Greenland between ~76 and 80°N (Gradmann & Ebbing, 2015). This gravity anomaly is matched by a similar, but smaller, gravity anomaly on the conjugate margin in Northern Norway (NN). Based on available geophysical and geological data and 3-D modeling of the lithospheric and sublithospheric mantle, Gradmann and Ebbing (2015) investigated the source of this anomaly in NN and concluded that a shallow crustal source would be most consistent with geophysical observations and isostatic considerations in Fennoscandia. The nature of this shallow source is difficult to constrain given the different regional geology of Fennoscandia and Greenland, but the authors suggest a thick layer of low-density granitic rocks as a plausible source for the NN gravity low. This low-density rock layer would have to be up to 20 km thick to explain the gravity low observed in NN (Olesen et al., 2002). However, a 20-km-thick granitic layer would elevate heat flow (Pascal et al., 2007) to a level incompatible with the relatively low GHF in NN (~50 to 60 mW/m^2) but more consistent with relatively high GHF estimates for NE Greenland. Rogozhina et al. (2016) estimated that GHF values range between 68 and 88 mW/m^2 in NEG and that the largest anomaly is located beneath the onset of NEGIS where high basal melting has been estimated (Fahnestock et al., 2001). In addition, GHF values ranging from 90 to

160 mW/m^2 have been estimated around the NorthGRIP ice core site (Buchardt & Dahl-Jensen, 2007; Dahl-Jensen, Gundestrup, et al., 2003; Greve, 2005; Rezvanbehbahani et al., 2017). A recent study by Rysgaard et al. (2018) also reported a GHF of 93 mW/m^2 in the Young Sound-Tyrolerfjord, a few degrees south of the strong gravity low, and suggested, based on the distribution of high GHF, that a geothermal heat source may exist beneath the central and northeastern parts of the GIS. The spatial extent, relative thickness, and shallow nature of the NELVZ (Figure 11—middle column and Figure 14—vertical profiles A-A′, B-B′, and E-E′) are compatible with evidence of elevated heat flow in central northern-northeastern Greenland and the potential presence of a thick and shallow low-density layer along the northeast Greenland margin, and we argue that the aforementioned geothermal heat source is most likely within the crust of NE Greenland.

Based on the above evidence and similarities (i.e., relative thickness and amplitude of the LVZs, high regional heat flow, and tectonic settings) between our study and previous tomography studies reporting evidence of midcrustal LVZs in stable cratonic regions (Chen et al., 2015; Gu & Shen, 2015; Yuan, 2015), we suggest that a thick, midcrustal, and regional-scale granitic layer formed under compressional tectonic settings during the closure of the Iapetus Ocean, and collision of Baltica and Laurentia is a potential source for the imaged NELVZ. The existence of granitic intrusion is supported by V_p/V_s ratio measurements from receiver function studies (Dahl-Jensen, Larsen et al., 2003; Kumar et al., 2007) favoring an overall felsic granitic crustal composition across NE Greenland (Christensen, 1996 – Table 3) and by field observations of glacial erratic suites across the Proterozoic-Phanerozoic platform of North Greenland that are characterized among other associated rocks by granitoid and gneiss clasts (Dawes et al., 2009). The averaged shear wave velocity within the NELVZ (from ~10- to 25-km depth) is consistent with shear wave velocities for granite-gneiss to granite-granodiorite rock types in this depth range (Christensen, 1996; Table 2). This hypothesis provides a common source for the gravity low observed in both NE Greenland and NN and could explain regional measurements of elevated heat flow if we consider the relative thickness of this granitic layer (Pascal et al., 2007) and the presence of high heat-producing granitoid rocks in NE Greenland as found in other Proterozoic terranes (Carson et al., 2014; Goodge, 2018; McLaren et al., 2003).

The reported extent of similar LVZ (Chen et al., 2015; Gu & Shen, 2015; Yuan, 2015) suggests, however, that this midcrustal granitic body does not extend far inland and is most likely concentrated along the northeast extent of the Caledonian fold belt. The localized scale of this granitic layer could explain why the strongest low-velocity anomaly is along the NE Greenland margin (~75 to 79°N and ~30 to 19°W) and is also consistent with the isolated nature of the NE Greenland gravity low. However, the hypothesis of a localized granitic source does not reflect the large scale of the NELVZ nor the spatial extent of high GHF in NE Greenland. But if we consider that the presence of an ~20-km-thick granitic layer in a crust of Paleoproterozoic tectonothermal ages can lead to crust-mantle boundary temperatures close to the melting point (Pascal et al., 2007), an argument can be made that an initially localized region of partial melt in the lower crust could have been enlarged by melt-rock interaction and melt intrusion inland and later crystallized/recrystallized to form a granite-rich midcrustal layer (Chen et al., 2015). The time frame of such a process remains, however, unclear. Another hypothesis, which could be developed further to test its viability, is that the migration of melt inland was facilitated through subsequent episodes of decompression melting in response to lithospheric unloading during deglaciation periods of the GIS (Stevens et al., 2016). These multiple episodes of crustal remelting and inland melt migration may also have led to a progressive fractionation of the crust in NE Greenland and regionally enhanced the migration of heat-producing elements to shallower depths (Korhonen & Johnson, 2015; Yuan, 2015). Variations in radiogenic heat generation and concentration could explain some of the variations in GHF across NE Greenland (Bachu, 1988; Carson et al., 2014; Goodge, 2018; McLaren et al., 2003). Similarly, local variations in the degree of granitic intrusions could contribute to the spatial variations in shear wave velocity observed in NE Greenland and explain the isolated nature of the NE Greenland gravity low.

While this scenario does not identify the detailed tectonic processes leading to the emplacement of a midcrustal granitic layer nor does it include the possible contribution of the Iceland plume to the NELVZ and elevated heat flow in NE Greenland, it strongly motivates more targeted studies in this region to better constrain the crustal composition, amplitude, and extent of the NELVZ. A higher-resolution model of the lithospheric structure beneath NE Greenland would also help better understand the mechanisms that are initiating NEGIS flow and controlling the glacier dynamics, helping reduce uncertainties in ice flow and ice sheet models.

5. Conclusion

We have combined ambient noise and earthquake dispersion measurements to derive broadband high-resolution group velocity maps from 8 to 170 s that we used to construct a 3-D shear wave velocity model of the lithospheric structure beneath Greenland and the surrounding regions. A Markov Chain Monte Carlo approach was used to explore the model space beneath Greenland and to estimate model uncertainties, which are used to identify robust velocity features. Resolution in the upper-to-mid crust and the upper mantle is good, but trade-offs between lower crust and uppermost mantle properties reduce model resolution in the 10 or so kilometers above and below the crust-mantle transition. Prominent features in the model include an upper-crustal SW-NE trending velocity change separating Greenland into two blocks of different tectonic history and crustal properties and a midcrustal low-velocity anomaly in NE Greenland underlying NEGIS and coincident with regions of elevated GHF. The spatial extent and amplitude of the NELVZ combined with previous geological and geophysical results in NE Greenland suggest that an important source of this crustal anomaly is most likely compositional. Deep and fast cratonic roots extend from southwestern to north-northwestern Greenland but are separated by a west to east oriented corridor of relatively low velocities across central Greenland. Relatively low upper mantle velocity also underlies the eastern Tertiary Basalt Province. The model suggests thinner lithosphere across central and central eastern Greenland, possibly from the passage of the Iceland plume, but limited thermal erosion of highly depleted cratonic keels in southwestern and north-northwestern Greenland.

Acknowledgments

This work was supported by the U.S. National Science Foundation (grants EAR-1246776 [partial M. P. and S. A.] and AGS-1338832 [R. A. and S. A.]) and by the Defense Threat Reduction Agency award HDTRA1-11-1-0027 (partial M. P. and C. A.). The time series and metadata used in this study are open access and available through the facilities of the IRIS DMC (IRIS Data Management System). When available, the DOI's for permanent and temporary networks used in this study have also been listed in the references (Albuquerque Seismological Laboratory (ASL)/USGS, 1988; GEOFON Data Centre, 1993; GEOSCOPE, 1982; Korea Polar Research Institute (KOPRI), 2013; Scripps Institution of Oceanography, 1986). IRIS is funded through the National Science Foundation through the Instrumentation and Facilities Program of the National Science Foundation under cooperative agreement EAR-1063471. The National Earthquake Information Center Advanced National Seismic System Comprehensive Catalog and the Global Centroid Moment Tensor Project Catalog were used to construct lists of earthquakes used in our analyses. A list of the regional and teleseismic events used to build our earthquake tomography model and our final 3-D shear wave velocity model (median model) are available in a digital form on the figshare data repository (doi: 10.6084/m9.figshare.6291074).

References

Albuquerque Seismological Laboratory (ASL)/USGS (1988). Global Seismograph Network (GSN-IRIS/USGS). International Federation of Digital Seismograph Networks. Other/Seismic Network. https://doi.org/10.7914/SN/IU

Alsulami, S., Paton, D. A., & Cornwell, D. G. (2015). Tectonic variation and structural evolution of the West Greenland continental margin. *AAPG Bulletin*, *99*(09), 1689–1711. https://doi.org/10.1306/03021514023

Amante, C., & Eakins, B. W. (2009). ETOPO1 1 arc-minute global relief model: Procedures, data sources and analysis (p. 19). Colorado: US Department of Commerce, National Oceanic and Atmospheric Administration, National Environmental Satellite, Data, and Information Service, National Geophysical Data Center, Marine Geology and Geophysics Division.

Anell, I., Thybo, H., & Artemieva, I. M. (2009). Cenozoic uplift and subsidence in the North Atlantic region: Geological evidence revisited. *Tectonophysics*, *474*(1–2), 78–105. https://doi.org/10.1016/j.tecto.2009.04.006

Artemieva, I. M., Billien, M., Lévêque, J. J., & Mooney, W. D. (2004). Shear wave velocity, seismic attenuation, and thermal structure of the continental upper mantle. *Geophysical Journal International*, *157*(2), 607–628. https://doi.org/10.1111/j.1365-246X.2004.02195.x

Artemieva, I. M., & Thybo, H. (2013). EUNAseis: A seismic model for Moho and crustal structure in Europe, Greenland, and the North Atlantic region. *Tectonophysics*, *609*, 97–153. https://doi.org/10.1016/j.tecto.2013.08.004

Aster, R. C., Borchers, B., & Thurber, C. H. (2005). *Parameter estimation and inverse problems*. Waltham: Elsevier Academic.

Bachu, S. (1988). Analysis of heat transfer processes and geothermal pattern in the Alberta Basin, Canada. *Journal of Geophysical Research*, *93*, 7767–7781. https://doi.org/10.1029/JB093iB07p07767

Bamber, J. L., Layberry, R. L., & Gogineni, S. P. (2001). A new ice thickness and bed data set for the Greenland ice sheet: 1. Measurement, data reduction, and errors. *Journal of Geophysical Research*, *106*, 33,773–33,780. https://doi.org/10.1029/2001JD900054

Barmin, M. P., Ritzwoller, M. H., & Levshin, A. L. (2001). A fast and reliable method for surface wave tomography. *Pure and Applied Geophysics*, *158*(8), 1351–1375. https://doi.org/10.1007/PL00001225

Bastow, I. D., Eaton, D. W., Kendall, J. M., Helffrich, G., Snyder, D. B., Thompson, D. A., et al. (2013). The Hudson Bay Lithospheric Experiment (HuBLE): Insights into Precambrian plate tectonics and the development of mantle keels. *Geological Society, London, Special Publications*, *389*, SP,389–SP,387.

Bensen, G. D., Ritzwoller, M. H., Barmin, M. P., Levshin, A. L., Lin, F., Moschetti, M. P., et al. (2007). Processing seismic ambient noise data to obtain reliable broad-band surface wave dispersion measurements. *Geophysical Journal International*, *169*(3), 1239–1260. https://doi.org/10.1111/j.1365-246X.2007.03374.x

Braun, A., Kim, H. R., Csatho, B., & von Frese, R. R. (2007). Gravity-inferred crustal thickness of Greenland. *Earth and Planetary Science Letters*, *262*(1-2), 138–158. https://doi.org/10.1016/j.epsl.2007.07.050

Brocher, T. M. (2005). Empirical relations between elastic wavespeeds and density in the Earth's crust. *Bulletin of the Seismological Society of America*, *95*(6), 2081–2092. https://doi.org/10.1785/0120050077

Brooks, C. K. (2011). The East Greenland rifted volcanic margin. *Geological Survey of Denmark and Greenland Bulletin*, *24*, 1–96.

Buchardt, S. L., & Dahl-Jensen, D. (2007). Estimating the basal melt rate at NorthGRIP using a Monte Carlo technique. *Annals of Glaciology*, *45*, 137–142. https://doi.org/10.3189/172756407782282435

Cammarano, F., Goes, S., Vacher, P., & Giardini, D. (2003). Inferring upper-mantle temperatures from seismic velocities. *Physics of the Earth and Planetary Interiors*, *138*(3–4), 197–222. https://doi.org/10.1016/S0031-9201(03)00156-0

Carson, C. J., McLaren, S., Roberts, J. L., Boger, S. D., & Blankenship, D. D. (2014). Hot rocks in a cold place: High sub-glacial heat flow in East Antarctica. *Journal of the Geological Society*, *171*(1), 9–12. https://doi.org/10.1144/jgs2013-030

Chalmers, J. A., & Pulvertaft, T. (2001). Development of the continental margins of the Labrador Sea: A review. *Geological Society of London, Special Publication*, *187*(1), 77–105. https://doi.org/10.1144/GSL.SP.2001.187.01.05

Chen, Y., Gu, Y. J., Dokht, R. M., & Sacchi, M. D. (2015). Crustal imprints of Precambrian orogenesis in western Laurentia. *Journal of Geophysical Research: Solid Earth*, *120*, 6993–7012. https://doi.org/10.1002/2014JB011353

Chian, D., & Louden, K. (1992). The structure of Archean-Ketilidian crust along the continental shelf of southwestern Greenland from a seismic refraction profile. *Canadian Journal of Earth Sciences*, *29*(2), 301–313. https://doi.org/10.1139/e92-027

Chian, D., & Louden, K. E. (1994). The continent-ocean crustal transition across the southwest Greenland margin. *Journal of Geophysical Research*, *99*, 9117–9135. https://doi.org/10.1029/93JB03404

Christensen, N. I. (1996). Poisson's ratio and crustal seismology. *Journal of Geophysical Research*, *101*, 3139–3156. https://doi.org/10.1029/95JB03446

Christensen, N. I., & Mooney, W. D. (1995). Seismic velocity structure and composition of the continental crust: A global view. *Journal of Geophysical Research*, *100*(B6), 9761–9788.

Clinton, J. F., Nettles, M., Walter, F., Anderson, K., Dahl-Jensen, T., Giardini, D., et al. (2014). Seismic network in Greenland monitors Earth and ice system. *Eos, Transactions American Geophysical Union*, *95*(2), 13–14. https://doi.org/10.1002/2014EO020001

Cuffey, K. M., & Patterson, W. S. B. (2010). *The physics of glaciers* (4th ed.). Cambridge, Mass: Academic.

Dahl-Jensen, D., Gundestrup, N., Gogineni, S. P., & Miller, H. (2003). Basal melt at NorthGRIP modeled from borehole, ice-core and radio-echo sounder observations. *Annals of Glaciology*, *37*, 207–212. https://doi.org/10.3189/172756403781815492

Dahl-Jensen, T., Larsen, T. B., Woelbern, I., Bach, T., Hanka, W., Kind, R., et al. (2003). Depth to Moho in Greenland: Receiver-function analysis suggests two Proterozoic blocks in Greenland. *Earth and Planetary Science Letters*, *205*(3-4), 379–393. https://doi.org/10.1016/S0012-821X(02)01080-4

Dahl-Jensen, T., Thybo, H., Hopper, J., & Rosing, M. (1998). Crustal structure at the SE Greenland margin from wide-angle and normal incidence seismic data. *Tectonophysics*, *288*(1-4), 191–198. https://doi.org/10.1016/S0040-1951(97)00292-8

Dahl-Jensen, T., Voss, P. H., & Larsen, T. B. (2016). Crustal structure over the Nagssugtoqidian deformation front in West Greenland: Receiver function analysis. *Geological Survey of Denmark and Greenland Bulletin*, *35*, 79–82.

Darbyshire, F. A., Dahl-Jensen, T., Larsen, T. B., Voss, P. H., & Joyal, G. (2017). Crust and uppermost-mantle structure of Greenland and the Northwest Atlantic from Rayleigh wave group velocity tomography. *Geophysical Journal International*, *212*(3), 1546–1569.

Darbyshire, F. A., Larsen, T. B., Mosegaard, K., Dahl-Jensen, T., Gudmundsson, O., Bach, T., et al. (2004). A first detailed look at the Greenland lithosphere and upper mantle, using Rayleigh wave tomography. *Geophysical Journal International*, *158*(1), 267–286. https://doi.org/10.1111/j.1365-246X.2004.02316.x

Dawes, P. R. (2009). The bedrock geology under the Inland Ice: The next major challenge for Greenland mapping. *Geological Survey of Denmark and Greenland Bulletin*, *17*, 57–60.

Døssing, A., Japsen, P., Watts, A. B., Nielsen, T., Jokat, W., Thybo, H., & Dahl-Jensen, T. (2016). Miocene uplift of the NE Greenland margin linked to plate tectonics: Seismic evidence from the Greenland Fracture Zone, NE Atlantic. *Tectonics*, *35*, 257–282. https://doi.org/10.1002/2015TC004079

Doubrovine, P. V., Steinberger, B., & Torsvik, T. H. (2012). Absolute plate motions in a reference frame defined by moving hot spots in the Pacific, Atlantic, and Indian oceans. *Journal of Geophysical Research*, *117*, B09101. https://doi.org/10.1029/2011JB009072

Dziewonski, A., Bloch, S., & Landisman, M. (1969). A technique for the analysis of transient seismic signals. *Bulletin of the Seismological Society of America*, *59*(1), 427–444.

Dziewonski, A. M., & Anderson, D. L. (1981). Preliminary reference Earth model. *Physics of the Earth and Planetary Interiors*, *25*(4), 297–356. https://doi.org/10.1016/0031-9201(81)90046-7

Ekström, G. (2011). A global model of Love and Rayleigh surface wave dispersion and anisotropy, 25-250 s. *Geophysical Journal International*, *187*(3), 1668–1686. https://doi.org/10.1111/j.1365-246X.2011.05225.x

Escher, J. C., & Pulvertaft, T. C. R. (1995). *Geological map of Greenland 1:2500000*. Copenhagen: Geological Survey of Greenland.

Fahnestock, M., Abdalati, W., Joughin, I., Brozena, J., & Gogineni, P. (2001). High geothermal heat flow, basal melt, and the origin of rapid ice flow in central Greenland. *Science*, *294*(5550), 2338–2342. https://doi.org/10.1126/science.1065370

Fullea, J., Afonso, J. C., Connolly, J. A. D., Fernandez, M., García-Castellanos, D., & Zeyen, H. (2009). LitMod3D: An interactive 3-D software to model the thermal, compositional, density, seismological, and rheological structure of the lithosphere and sublithospheric upper mantle. *Geochemistry, Geophysics, Geosystems*, *10*, Q08019. https://doi.org/10.1029/2009GC002391

Funck, T., Erlendsson, Ö., Geissler, W. H., Gradmann, S., Kimbell, G. S., McDermott, K., & Petersen, U. K. (2017). A review of the NE Atlantic conjugate margins based on seismic refraction data. *Geological Society, London, Special Publications*, *447*(1), 171–205. https://doi.org/10.1144/SP447.9

GEOFON Data Centre (1993). GEOFON Seismic Network. Deutsches GeoForschungsZentrum GFZ. Other/Seismic Network. https://doi.org/10.14470/TR560404

GEOSCOPE (1982). French Global Network of Broad Band Seismic Stations. Institut de Physique du Globe de Paris (IPGP). https://doi.org/10.18715/GEOSCOPE.G

Goes, S., Govers, R., & Vacher, P. (2000). Shallow mantle temperatures under Europe from *P* and *S* wave tomography. *Journal of Geophysical Research*, *105*, 11,153–11,169. https://doi.org/10.1029/1999JB900300

Goodge, J. W. (2018). Crustal heat production and estimate of terrestrial heat flow in central East Antarctica, with implications for thermal input to the East Antarctic ice sheet. *The Cryosphere*, *12*(2), 491–504. https://doi.org/10.5194/tc-12-491-2018

Gradmann, S., & Ebbing, J. (2015). Large-scale gravity anomaly in northern Norway: Tectonic implications of shallow or deep source depth and a possible conjugate in northeast Greenland. *Geophysical Supplements to the Monthly Notices of the Royal Astronomical Society*, *203*(3), 2070–2088. https://doi.org/10.1093/gji/ggv426

Greve, R. (2005). Relation of measured basal temperatures and the spatial distribution of the geothermal heat flux for the Greenland ice sheet. *Annals of Glaciology*, *42*, 424–432. https://doi.org/10.3189/172756405781812510

Gu, Y. J., & Shen, L. (2015). Noise correlation tomography of Southwest Western Canada Sedimentary Basin. *Geophysical Journal International*, *202*(1), 142–162. https://doi.org/10.1093/gji/ggv100

Hamann, N. E., Whittaker, R. C., & Stemmerik, L. (2005, January). Geological development of the Northeast Greenland shelf. In *Geological Society, London, Petroleum Geology Conference series*. *Geological Society of London*, *6*(1), 887–902.

Henriksen, N., Chalmers, J. A., & Friend, C. R. (2008). Geological history of Greenland: Four billion years of Earth evolution. Geological Survey of Denmark and Greenland.

Henriksen, N., Higgins, A. K., Kalsbeek, F., & Pulvertaft, T. C. R. (2009). Greenland from Archaean to Quaternary. *Geological Survey of Denmark and Greenland Bulletin*, *18*, 126.

Hermann, T., & Jokat, W. (2016). Crustal structure off Kong Oscar Fjord, east Greenland: Evidence for focused melt supply along the Jan Mayen fracture zone. *Tectonophysics*, *691*, 110–119. https://doi.org/10.1016/j.tecto.2015.12.005

Herrmann, R. B. (2013). Computer programs in seismology: An evolving tool for instruction and research. *Seismological Research Letters*, *84*(6), 1081–1088. https://doi.org/10.1785/0220110096

Holbrook, W. S., Larsen, H., Korenaga, J., Dahl-Jensen, T., Reid, I. D., Kelemen, P., et al. (2001). Mantle thermal structure and active upwelling during continental breakup in the North Atlantic. *Earth and Planetary Science Letters*, *190*(3-4), 251–266. https://doi.org/10.1016/S0012-821X(01)00392-2

Hopper, J. R., Dahl-Jensen, T., Holbrook, W. S., Larsen, H. C., Lizarralde, D., Korenaga, J., et al. (2003). Structure of the SE Greenland margin from seismic reflection and refraction data: Implications for nascent spreading center subsidence and asymmetric crustal accretion during North Atlantic opening. *Journal of Geophysical Research*, *108*(B5), 2269. https://doi.org/10.1029/2002JB001996

Jakovlev, A. V., Bushenkova, N. A., Koulakov, I. Y., & Dobretsov, N. L. (2012). Structure of the upper mantle in the Circum-Arctic region from regional seismic tomography. *Russian Geology and Geophysics*, *53*(10), 963–971. https://doi.org/10.1016/j.rgg.2012.08.001

Japsen, P., & Chalmers, J. A. (2000). Neogene uplift and tectonics around the North Atlantic: Overview. *Global and Planetary Change*, *24*(3-4), 165–173. https://doi.org/10.1016/S0921-8181(00)00006-0

Japsen, P., Green, P. F., Bonow, J. M., Nielsen, T. F., & Chalmers, J. A. (2014). From volcanic plains to glaciated peaks: Burial, uplift and exhumation history of southern East Greenland after opening of the NE Atlantic. *Global and Planetary Change*, *116*, 91–114. https://doi.org/10.1016/j.gloplacha.2014.01.012

Kao, H., Behr, Y., Currie, C. A., Hyndman, R., Townend, J., Lin, F. C., et al. (2013). Ambient seismic noise tomography of Canada and adjacent regions: Part I. Crustal structures. *Journal of Geophysical Research: Solid Earth*, *118*, 5865–5887. https://doi.org/10.1002/2013JB010535

Keen, C. E., Dickie, K., & Dehler, S. A. (2012). The volcanic margins of the northern Labrador Sea: Insights to the rifting process. *Tectonics*, *31*, TC1011. https://doi.org/10.1029/2011TC002985

Kennett, B. L. N., Engdahl, E. R., & Buland, R. (1995). Constraints on seismic velocities in the Earth from traveltimes. *Geophysical Journal International*, *122*(1), 108–124. https://doi.org/10.1111/j.1365-246X.1995.tb03540.x

Khan, S. A., Sasgen, I., Bevis, M., van Dam, T., Bamber, J. L., Wahr, J., et al. (2016). Geodetic measurements reveal similarities between post–Last Glacial Maximum and present-day mass loss from the Greenland ice sheet. *Science Advances*, *2*(9), e1600931. https://doi.org/10.1126/sciadv.1600931

Koch, L., & Haller, J. (1971). Geological map of East Greenland 72°–76° N. lat.: de Danske ekspeditioner til Østgrønland 1947-58. Reitzel.

Korea Polar Research Institute (KOPRI) (2013). Korea Polar Observation Seismic Network. International Federation of Digital Seismograph Networks. Other/Seismic Network. https://doi.org/10.7914/SN/KP

Korenaga, J., Holbrook, W. S., Kent, G. M., Kelemen, P. B., Detrick, R. S., Larsen, H. C., et al. (2000). Crustal structure of the southeast Greenland margin from joint refraction and reflection seismic tomography. *Journal of Geophysical Research*, *105*, 21,591–21,614. https://doi.org/10.1029/2000JB900188

Korhonen, F. J., & Johnson, S. P. (2015). The role of radiogenic heat in prolonged intraplate reworking: The Capricorn Orogen explained? *Earth and Planetary Science Letters*, *428*, 22–32. https://doi.org/10.1016/j.epsl.2015.06.039

Kraft, H. A., Vinnik, L., & Thybo, H. (2018). Mantle transition zone beneath central-eastern Greenland: Possible evidence for a deep tectosphere from receiver functions. *Tectonophysics*, *728*, 34–40.

Kumar, P., Kind, R., Hanka, W., Wylegalla, K. R. C. H., Reigber, C., Yuan, X., et al. (2005). The lithosphere–asthenosphere boundary in the North-West Atlantic region. *Earth and Planetary Science Letters*, *236*(1-2), 249–257. https://doi.org/10.1016/j.epsl.2005.05.029

Kumar, P., Kind, R., Priestley, K., & Dahl-Jensen, T. (2007). Crustal structure of Iceland and Greenland from receiver function studies. *Journal of Geophysical Research*, *112*, B03301. https://doi.org/10.1029/2005JB003991

Larour, E., Morlighem, M., Seroussi, H., Schiermeier, J., & Rignot, E. (2012). Ice flow sensitivity to geothermal heat flux of Pine Island Glacier, Antarctica. *Journal of Geophysical Research*, *117*, F04023. https://doi.org/10.1029/2012JF002371

Larsen, H. C. (1990). The East Greenland Shelf. In A. Grantz, L. Johnson, & J. F. Sweeney (Eds.), *The Arctic Ocean Region. The geology of North America, Vol. L*, (pp. I85–I210). Boulder, CO: Geological Society of America.

Larsen, H. C., & Saunders, A. D. (1998). 41. Tectonism and volcanism at the southeast Greenland rifted margin: A record of plume impact and later continental rupture. *Proceeding of the Ocean Drilling Program, Scientific Results*, *152*, 503–533.

Larsen, L. M., Pedersen, A. K., Tegner, C., & Duncan, R. A. (2014). Eocene to Miocene igneous activity in NE Greenland: Northward younging of magmatism along the East Greenland margin. *Journal of the Geological Society*, *171*(4), 539–553. https://doi.org/10.1144/jgs2013-118

Larsen, T. B., Yuen, D. A., & Storey, M. (1999). Ultrafast mantle plumes and implications for flood basalt volcanism in the Northern Atlantic Region. *Tectonophysics*, *311*(1-4), 31–43. https://doi.org/10.1016/S0040-1951(99)00163-8

Laske, G., Masters, G., Ma, Z., & Pasyanos, M. E. (2013). A new global crustal model at 1 × 1 degrees (CRUST1. 0).

Lawver, L. A., & Müller, R. D. (1994). Iceland hotspot track. *Geology*, *22*(4), 311–314. https://doi.org/10.1130/0091-7613(1994)022<0311:IHT>2.3.CO;2

Lebedev, S., Schaeffer, A. J., Fullea, J., & Pease, V. (2017). Seismic tomography of the Arctic region: Inferences for the thermal structure and evolution of the lithosphere. *Geological Society, London, Special Publications*, *460*, SP,460–SP,410.

Lecocq, T., Caudron, C., & Brenguier, F. (2014). MSNoise, a python package for monitoring seismic velocity changes using ambient seismic noise. *Seismological Research Letters*, *85*(3), 715–726. https://doi.org/10.1785/0220130073

Lekic, V., & Romanowicz, B. (2011). Tectonic regionalization without a priori information: A cluster analysis of upper mantle tomography. *Earth and Planetary Science Letters*, *308*(1-2), 151–160. https://doi.org/10.1016/j.epsl.2011.05.050

Levshin, A., Shen, W., Barmin, M., & Ritzwoller, M. (2017) Surface wave studies of the Greenland upper lithosphere using ambient seismic noise.

McLaren, S., Sandiford, M., Hand, M., Neumann, N., Wyborn, L., & Bastrakova, I. (2003). The hot southern continent: Heat flow and heat production in Australian Proterozoic terranes. *Special Papers-geological Society of America*, 157–168. https://doi.org/10.1130/0-8137-2372-8.157

Mordret, A. (2018). Uncovering the Iceland hotspot track beneath Greenland. *Journal of Geophysical Research*, *123*, 4922–4941. https://doi.org/10.1029/2017JB015104

Morgan, W. J. (1983). Hotspot tracks and the early rifting of the Atlantic. *Tectonophysics*, *94*(1–4), 123–139. https://doi.org/10.1016/0040-1951(83)90013-6

Mosegaard, K., & Tarantola, A. (1995). Monte Carlo sampling of solutions to inverse problems. *Journal of Geophysical Research*, *100*, 12,431–12,447. https://doi.org/10.1029/94JB03097

Müller, R. D., Royer, J. Y., & Lawver, L. A. (1993). Revised plate motions relative to the hotspots from combined Atlantic and Indian Ocean hotspot tracks. *Geology*, *21*(3), 275–278. https://doi.org/10.1130/0091-7613(1993)021<0275:RPMRTT>2.3.CO;2

Nettles, M. (2014). Understanding Precambrian to Present Assembly of Greenland. International Federation of Digital Seismograph Networks. Other/Seismic Network.doi:https://doi.org/10.7914/SN/XF_2014

Nielsen, T. K., Larsen, H. C., & Hopper, J. R. (2002). Contrasting rifted margin styles south of Greenland: Implications for mantle plume dynamics. *Earth and Planetary Science Letters*, *200*(3-4), 271–286. https://doi.org/10.1016/S0012-821X(02)00616-7

Olesen, O., Lundin, E., Nordgulen, Ø., Osmundsen, P. T., Skilbrei, J. R., Smethurst, M. A., et al. (2002). Bridging the gap between the onshore and offshore geology in Nordland, northern Norway. *Norwegian Journal of Geology/Norsk Geologisk Forening*, *82*(4), 243–262.

O'Neill, C., Müller, D., & Steinberger, B. (2005). On the uncertainties in hot spot reconstructions and the significance of moving hot spot reference frames. *Geochemistry, Geophysics, Geosystems*, *6*, Q04003. https://doi.org/10.1029/2004GC000784

Pascal, C., Ebbing, J., & Skilbrei, J. R. (2007). Interplay between the Scandes and the trans-Scandinavian igneous belt: Integrated thermo-rheological and potential field modelling of the Central Scandes profile. *Norwegian Journal of Geology/Norsk Geologisk Forening*, *87*, 3–12.

Peace, A. L., Foulger, G. R., Schiffer, C., & McCaffrey, K. J. (2017). Evolution of Labrador Sea–Baffin Bay: Plate or plume processes? *Geoscience Canada*, *44*(3), 91–102. https://doi.org/10.12789/geocanj.2017.44.120

Petrov, O., Morozov, A., Shokalsky, S., Kashubin, S., Artemieva, I. M., Sobolev, N., et al. (2016). Crustal structure and tectonic model of the Arctic region. *Earth-Science Reviews*, *154*, 29–71. https://doi.org/10.1016/j.earscirev.2015.11.013

Petrunin, A. G., Rogozhina, I., Vaughan, A. P. M., Kukkonen, I. T., Kaban, M. K., Koulakov, I., & Thomas, M. (2013). Heat flux variations beneath central Greenland/'s ice due to anomalously thin lithosphere. *Nature Geoscience*, *6*(9), 746–750. https://doi.org/10.1038/ngeo1898

Pilidou, S., Priestley, K., Gudmundsson, O., & Debayle, E. (2004). Upper mantle S-wave speed heterogeneity and anisotropy beneath the North Atlantic from regional surface wave tomography: The Iceland and Azores plumes. *Geophysical Journal International*, *159*(3), 1057–1076. https://doi.org/10.1111/j.1365-246X.2004.02462.x

Pollard, D., DeConto, R. M., & Nyblade, A. A. (2005). Sensitivity of Cenozoic Antarctic ice sheet variations to geothermal heat flux. *Global and Planetary Change*, *49*(1-2), 63–74. https://doi.org/10.1016/j.gloplacha.2005.05.003

Pourpoint, M., Anandakrishnan, S., & Ammon, C. J. (2018). High resolution Rayleigh-wave group velocity variation beneath Greenland. *Journal of Geophysical Research: Solid Earth*, *123*, 1516–1539. https://doi.org/10.1002/2017JB015072

Priestley, K., & McKenzie, D. (2006). The thermal structure of the lithosphere from shear wave velocities. *Earth and Planetary Science Letters*, *244*(1–2), 285–301. https://doi.org/10.1016/j.epsl.2006.01.008

Ramberg, H. (1949). On the petrogenesis of the gneiss complexes between Sukkertoppen and Christianshaab, West Greenland. *Meddelelser fra Dansk Geologisk Forening*, *11*, 312–327.

Rezvanbehbahani, S., Stearns, L. A., Kadivar, A., Walker, J. D., & van der Veen, C. J. (2017). Predicting the geothermal heat flux in Greenland: A machine learning approach. *Geophysical Research Letters*, *44*, 12,271–12,279. https://doi.org/10.1002/2017GL075661

Rickers, F., Fichtner, A., & Trampert, J. (2013). The Iceland–Jan Mayen plume system and its impact on mantle dynamics in the North Atlantic region: Evidence from full-waveform inversion. *Earth and Planetary Science Letters*, *367*, 39–51. https://doi.org/10.1016/j.epsl.2013.02.022

Ritzwoller, M. H., Shapiro, N. M., Levshin, A. L., & Leahy, G. M. (2001). Crustal and upper mantle structure beneath Antarctica and surrounding oceans. *Journal of Geophysical Research*, *106*, 30,645–30,670. https://doi.org/10.1029/2001JB000179

Roberts, D. G., & Bally, A. W. (Eds.) (2012). *Regional geology and tectonics: Phanerozoic passive margins, cratonic basins and global tectonic maps*. Heidelberg: Elsevier.

Rogozhina, I., Petrunin, A. G., Vaughan, A. P., Steinberger, B., Johnson, J. V., Kaban, M. K., et al. (2016). Melting at the base of the Greenland ice sheet explained by Iceland hotspot history. *Nature Geoscience*, *9*(5), 366–369. https://doi.org/10.1038/ngeo2689

Rysgaard, S., Bendtsen, J., Mortensen, J., & Sejr, M. K. (2018). High geothermal heat flux in close proximity to the Northeast Greenland Ice Stream. *Scientific Reports*, *8*(1), 1344. https://doi.org/10.1038/s41598-018-19244-x

Schaeffer, A. J., & Lebedev, S. (2013). Global shear speed structure of the upper mantle and transition zone. *Geophysical Journal International*, *194*(1), 417–449. https://doi.org/10.1093/gji/ggt095

Schaeffer, A. J., & Lebedev, S. (2014). Imaging the North American continent using waveform inversion of global and USArray data. *Earth and Planetary Science Letters*, *402*, 26–41. https://doi.org/10.1016/j.epsl.2014.05.014

Schiffer, C., Jacobsen, B. H., Balling, N., Ebbing, J., & Nielsen, S. B. (2015). The East Greenland Caledonides—Teleseismic signature, gravity and isostasy. *Geophysical Journal International*, *203*(2), 1400–1418. https://doi.org/10.1093/gji/ggv373

Schiffer, C., Tegner, C., Schaeffer, A. J., Pease, V., & Nielsen, S. B. (2018). High Arctic geopotential stress field and implications for geodynamic evolution. *Geological Society, London, Special Publications*, *460*(1), 441–465. https://doi.org/10.1144/SP460.6

Schlindwein, V., & Jokat, W. (1999). Structure and evolution of the continental crust of northern east Greenland from integrated geophysical studies. *Journal of Geophysical Research*, *104*, 15,227–15,245. https://doi.org/10.1029/1999JB900101

Schmidt-Aursch, M. C., & Jokat, W. (2005). The crustal structure of central East Greenland: From the Caledonian orogen to the Tertiary igneous province. *Geophysical Journal International*, *160*(2), 736–752. https://doi.org/10.1111/j.1365-246X.2005.02514.x

Schoonman, C. M., White, N. J., & Pritchard, D. (2017). Radial viscous fingering of hot asthenosphere within the Icelandic plume beneath the North Atlantic Ocean. *Earth and Planetary Science Letters*, *468*, 51–61. https://doi.org/10.1016/j.epsl.2017.03.036

Scripps Institution of Oceanography (1986). IRIS/IDA Seismic Network. International Federation of Digital Seismograph Networks.Other/Seismic Network. https://doi.org/10.7914/SN/II

Shapiro, N. M., & Ritzwoller, M. H. (2002). Monte-Carlo inversion for a global shear-velocity model of the crust and upper mantle. *Geophysical Journal International*, *151*(1), 88–105. https://doi.org/10.1046/j.1365-246X.2002.01742.x

Shen, W., Ritzwoller, M. H., Schulte-Pelkum, V., & Lin, F. C. (2012). Joint inversion of surface wave dispersion and receiver functions: A Bayesian Monte-Carlo approach. *Geophysical Journal International*, *192*(2), 807–836.

Sleep, N. H. (1997). Lateral flow and ponding of starting plume material. *Journal of Geophysical Research*, *102*, 10,001–10,012. https://doi.org/10.1029/97JB00551

Sleep, N. H., Ebinger, C. J., & Kendall, J. M. (2002). Deflection of mantle plume material by cratonic keels. *Geological Society, London, Special Publications*, *199*(1), 135–150. https://doi.org/10.1144/GSL.SP.2002.199.01.08

Steffen, R., Strykowski, G., & Lund, B. (2017). High-resolution Moho model for Greenland from EIGEN-6C4 gravity data. *Tectonophysics*, *706-707*, 206–220. https://doi.org/10.1016/j.tecto.2017.04.014

Steinberger, B., Spakman, W., Japsen, P., & Torsvik, T. H. (2015). The key role of global solid-Earth processes in preconditioning Greenland's glaciation since the Pliocene. *Terra Nova*, *27*(1), 1–8. https://doi.org/10.1111/ter.12133

Steinberger, B., Sutherland, R., & O'connell, R. J. (2004). Prediction of Emperor-Hawaii seamount locations from a revised model of global plate motion and mantle flow. *Nature*, *430*(6996), 167–173. https://doi.org/10.1038/nature02660

Stemmerik, L., Christiansen, F. G., Piasecki, S., Jordt, B., Marcussen, C., & Nøhr-Hansen, H. (2013, October). Depositional history and petroleum geology of the Carboniferous to Cretaceous sediments in the northern part. In *Arctic Geology and Petroleum Potential: Proceedings of the Norwegian Petroleum Society Conference, 15–17 August 1990, Tromso, Norway* (Vol. 2, p. 66). Elsevier.

Stephenson, R., Oakey, G. N., Schiffer, C., & Jacobsen, B. H. (2013). Ellesmere Island Lithosphere xperiment (ELLITE): Eurekan basin inversion and mountain building, Ellesmere Island, Nunavut. *Geological Survey of Canada, Current Research*, *21*. https://doi.org/10.4095/292859

Stevens, N. T., Parizek, B. R., & Alley, R. B. (2016). Enhancement of volcanism and geothermal heat flux by ice-age cycling: A stress modeling study of Greenland. *Journal of Geophysical Research: Earth Surface*, *121*, 1456–1471. https://doi.org/10.1002/2016JF003855

Storey, M., Duncan, R. A., & Swisher, C. C. (2007). Paleocene-Eocene thermal maximum and the opening of the northeast Atlantic. *Science*, *316*(5824), 587–589. https://doi.org/10.1126/science.1135274

Surlyk, F. (1990). Timing, style and sedimentary evolution of Late Palaeozoic-Mesozoic extensional basins of East Greenland. *Geological Society, London, Special Publications*, *55*(1), 107–125. https://doi.org/10.1144/GSL.SP.1990.055.01.05

Tsikalas, F., Faleide, J. I., Eldholm, O., & Wilson, J. (2005, January). Late Mesozoic–Cenozoic structural and stratigraphic correlations between the conjugate mid-Norway and NE Greenland continental margins. In *Geological Society, London, Petroleum Geology Conference series*. *Geological Society of London*, *6*(1), 785–801.

Upton, B. G. J. (1988). History of Tertiary igneous activity in the N Atlantic borderlands. *Geological Society, London, Special Publications*, *39*(1), 429–453. https://doi.org/10.1144/GSL.SP.1988.039.01.38

van Gool, J. A., Alsop, G. I., Árting, U. E., Garde, A. A., Knudsen, C., Krawiec, A. W., et al. (2002). Precambrian geology of the northern Nagssugtoqidian orogen, West Greenland: Mapping in the Kangaatsiaq area. *Geology of Greenland Survey Bulletin*, *191*, 13–23.

van Gool, J. A., Connelly, J. N., Marker, M., & Mengel, F. C. (2002). The Nagssugtoqidian Orogen of West Greenland: Tectonic evolution and regional correlations from a West Greenland perspective. *Canadian Journal of Earth Sciences*, *39*(5), 665–686. https://doi.org/10.1139/e02-027

Voss, M., & Jokat, W. (2007). Continent-ocean transition and voluminous magmatic underplating derived from P-wave velocity modelling of the East Greenland continental margin. *Geophysical Journal International*, *170*(2), 580–604. https://doi.org/10.1111/j.1365-246X.2007.03438.x

Voss, M., Schmidt-Aursch, M. C., & Jokat, W. (2009). Variations in magmatic processes along the East Greenland volcanic margin. *Geophysical Journal International*, *177*(2), 755–782. https://doi.org/10.1111/j.1365-246X.2009.04077.x

Wardle, R. J., Scott, D., van Gool, J., Garde, A., Culshaw, N., & Hall, J. (2000). An overview of the development of NE Laurentia: Nain-Superior collision and links to western Trans-Hudson Orogen. Abstract Volume (Geological Association of Canada).

Yang, Y., & Ritzwoller, M. H. (2008). Characteristics of ambient seismic noise as a source for surface wave tomography. *Geochemistry, Geophysics, Geosystems*, *9*, Q02008. https://doi.org/10.1029/2007GC001814

Yuan, H. (2015). Secular change in Archaean crust formation recorded in Western Australia. *Nature Geoscience*, *8*(10), 808–813. https://doi.org/10.1038/ngeo2521

Zwally, H. J., Giovinetto, M. B., Beckley, M. A., & Saba, J. L. (2012). Antarctic and Greenland drainage systems. *GSFC Cryospheric Sciences Laboratory*.